Architecture, deformation style and petrophysical properties of growth fault systems: the Late Triassic deltaic succession of southern Edgeøya (East Svalbard)

Kei Ogata[1] | **Mark J. Mulrooney**[2,3] | **Alvar Braathen**[3] | **Harmon Maher**[4] | **Per Terje Osmundsen**[5] | **Ingrid Anell**[3] | **Aleksandra Anna Smyrak-Sikora**[2,6] | **Fabrizio Balsamo**[7]

[1]Faculty of Science, Geology and Geochemistry Cluster, VU Amsterdam, Amsterdam, the Netherlands

[2]Department of Arctic Geology, University Centre in Svalbard, Svalbard, Norway

[3]Department of Geosciences, University of Oslo, Oslo, Norway

[4]Department of Geography and Geology, University of Nebraska at Omaha, Omaha, NE, USA

[5]Geological Survey of Norway, Trondheim, Norway

[6]Department of Earth Science, University of Bergen, Bergen, Norway

[7]NEXT - Natural and Experimental Tectonics Research Group, Department of Chemistry, Life Sciences and Environmental Sustainability, University of Parma, Parma, Italy

Correspondence
Kei Ogata, Faculty of Science, Geology and Geochemistry Cluster, VU Amsterdam, Amsterdam, the Netherlands.
Email: k.ogata@vu.nl

Funding information
Petromaks Trias North Project, Grant/Award Number: 234152/E30; Research Council of Norway; Edison Norway; Lundin Norway; RWE Dea Norge; Statoil and Tullow Oil

Abstract

The Late Triassic outcrops on southern Edgeøya, East Svalbard, allow a multiscale study of syn-sedimentary listric growth faults located in the prodelta region of a regional prograding system. At least three hierarchical orders of growth faults have been recognized, each showing different deformation mechanisms, styles and stratigraphic locations of the associated detachment interval. The faults, characterized by mutually influencing deformation envelopes over space-time, generally show SW- to SE-dipping directions, indicating a counter-regional trend with respect to the inferred W-NW directed progradation of the associated delta system. The down-dip movement is accommodated by polyphase deformation, with the different fault architectural elements recording a time-dependent transition from fluidal-hydroplastic to ductile-brittle deformation, which is also conceptually scale-dependent, from the smaller- (3rd order) to the larger-scale (1st order) end-member faults respectively. A shift from distributed strain to strain localization towards the fault cores is observed at the meso to micro-scale (<1 mm), and in the variation in petrophysical parameters of the litho-structural facies across and along the fault envelope, with bulk porosity, density, pore size and microcrack intensity varying accordingly to deformation and reworking intensity of inherited structural fabrics. The second- and third-order listric fault nucleation points appear to be located above blind fault tip-related monoclines involving cemented organic shales. Close to planar, through-going, first-order faults cut across this boundary, eventually connecting with other favourable lower-hierarchy fault to create seismic-scale fault zones similar to those imaged in the nearby offshore areas. The inferred large-scale driving mechanisms for the first-order faults are related to the combined effect of tectonic reactivation of deeper Palaeozoic structures in a far field stress regime due to the Uralide orogeny, and differential compaction associated with increased sand sedimentary input in a fine-grained, water-saturated, low-accommodation, prodeltaic depositional environment. In synergy to this large-scale picture, small-scale causative factors favouring second- and third-order faulting seem to be related to mechanical-rheological instabilities related to localized shallow diagenesis and liquidization fronts.

1 | INTRODUCTION

Extensional, listric growth faults are commonly observed in deltaic settings, where sand-rich sedimentary sequences prograde out over prodelta shales causing overpressure and density disequilibria. Such faults have been identified at various scales in the ancient (e.g. Bhattacharya & Davies, 2001; Callot et al., 2009; Edwards, 1976; Nemec et al., 1988; Rider, 1978; Wignall & Best, 2004) and the modern sedimentary record (e.g. Cohen & McClay, 1996; Damuth, 1994; Imber et al., 2003; Maestro, Barnolas, Somoza, Lowrie, & Lawton, 2002; Yeager et al., 2012). Syn-sedimentary faults can occur over widespread areas from the upper delta slope to the delta top, and inland, up to the distal alluvial plain, usually showing strike directions roughly parallel to the coastline and delta lobe contours (Back, Jing, Thang, & Morley, 2005; Pochat, Castelltort, vanden Driessche, Besnard, & Gumiaux, 2004). Such systems are commonly associated with compressional zones basin-ward, commonly located at the delta toe (i.e. base of the delta slope), with the development of mid- to deep-water "fold-and-thrust belts," defined as toe-thrust zones (see e.g. Mandl & Crans, 1981). This general arrangement is not always observed, and in several cases the growth faults domains are bounded by counter-regional, landward dipping, large-scale listric faults (Pochat et al., 2004; Rouby, Raillard, Guillocheau, Bouroullec, & Nalpas, 2002; Sapin, Ringenbach, Rives, & Pubellier, 2012), a pattern also replicated in analogue models (McClay, Dooley, & Lewis, 1998; McClay & Ellis, 1987). Such situations have been related to local to regional differential compaction and sedimentary loading between the finer, water-saturated outer prodelta and the inner, coarser delta front-top zones (Back & Morley, 2016; Braathen et al., 2017).

The practical importance of these structures to hydrocarbon exploration and production, hydrogeological exploitation and geohazard assessment (e.g. mitigation of coastal instability and land loss prediction) is well known (e.g. Armstrong, Mohrig, Hess, George, & Straub, 2014; Gagliano, 2005). Their large-scale, structural and stratigraphic characteristics have been largely revealed by remote-sensing, acoustic and seismic imaging, mainly because of the impact of changing fault dips, and marked impedance of the related fault rock types on the seismic signal (Back & Morley, 2016; King, Backé, Morley, Hillis, & Tingay, 2010; Panpichityota, Morley, & Ghosh, 2018). Field-based studies, specifically aimed to provide insights on the micro to mesoscale (i.e. from less than 1 mm to the size of the outcrop) syn-sedimentary deformation mechanisms of growth faulting at shallow crustal conditions (< than 1 km burial), are underrepresented in the current literature, partially due to the relative scarcity of favourable exposures. A few exceptions are available (Bhattacharya & Davies, 2001; Bouroullec et al., 2004; Braathen et al., 2017; Onderdonk & Midtkandal, 2010; Zecchin, Massari, Mellere, & Prosser, 2003), and usually describe neo-tectonic faulting in poorly consolidated lithologies (Bense & Person, 2006; Heynekamp, Goodwin, Mozley, & Haneberg, 1999; Loveless, Bense, & Turner, 2011; Mozley & Goodwin, 1995; Rawling & Goodwin, 2003, 2006). This outcrop-based study presents the results of a combined structural-stratigraphic and petrophysical analysis the superbly exposed, Late Triassic growth fault system cropping out in the southern part of Edgeøya, Svalbard (Arctic Norway). The main objective of this study was to provide a high-resolution, multiscale characterization of these growth fault architectures and structural elements, in order to understand: (1) the primary deformation mechanisms and their control on petrophysical properties, (2) their associated spatial-temporal variations and structural diagenesis and (3) identify local (i.e. autogenic) and regional (i.e. allogenic) factors that influenced fault nucleation and growth.

Highlights

- The Triassic growth fault systems of southern Edgeøya comprise three orders of faults, from deep-rooted planar faults to shallow listric faults;
- Polyphase deformation from soft-sediment to brittle deformation from first-order to third-order faults
- Variation in the growth fault architectural elements and intrinsic petrophysical properties across and along the fault zones;
- Counter-regional (landward), progressive faulting in prodelta region due to cobine far-field stress and differential compaction;

2 | GEOLOGIC OUTLINE

Edgeøya is the second largest island of the Svalbard archipelago and is located in its eastern part (Figure 1a,b). The

Svalbard archipelago is the emergent, uplifted, northwestern margin of the Barents Shelf, with a geological record that includes: (1) the Caledonian Orogeny (and older events; Braathen et al., 1999), (2) Devonian crustal-scale extension and later contraction, (3) Carboniferous rifting, (4) a relatively stable, long-term subsiding platform sedimentation from Permian to Cretaceous with Late Triassic compression and regional uplift (Klausen, Müller, Slama, & Helland-Hansen, 2016), (5) intrusive, mafic Late Cretaceous magmatism of the High Arctic Large Igneous Province (HALIP, see Maher, 2001; Senger, Tveranger, Ogata, Braathen, & Planke, 2014) and (vi) development of a Cenozoic transform margin (e.g. Harland, 1997). The emergence of the Svalbard archipelago above sea level is the combined product of: (1) Early Cretaceous magmatism and the associated uplift and unroofing in the northwestern Barents Shelf, (2) development of the WSFTB, (3) uplift and unroofing in the western areas during the Oligocene and eventually (4) rapid, glacial isostatic-rebound during the Quaternary, which caused unroofing and consequent decompaction of the sedimentary succession (Corfu, Andersen, & Gasser, 2014; Minakov, Faleide, Glebovsky, & Mjelde, 2012; Nejbert, Krajewski, Dubinska, & Pecskay, 2011; Senger et al., 2014). On a larger scale, this part of the Barents Shelf is thought to represent a broad foreland setting bound by two opposite orogenic fronts, the Ordovician-Devonian Caledonides roughly to the W and the Carboniferous-Permian Uralides approximately to the E/SE (along with its Middle-Late Triassic/Jurassic indentations/protrusions represented by Novaya Zemlya), which caused curvilinear trends of the stress trajectories and a complex interaction of the foreland deformation patterns (Lyberis & Manby, 1999; Marello, J. Ebbing, & Gernigon, 2013; Scott, Howard, Guo, Schekoldin, & Pease, 2011).

Edgeøya comprises of a conformable Middle-Late Triassic succession, which contain the uppermost and lowermost parts of the Sassendalen and Kapp Toscana Groups respectively (Figure 1c,d; Dallmann et al., 1999). The lithologies within the lower part of the cliff sections belong to the Ladinian Blanknuten Member of the Botneheia Formation (Sassendalen Grp.), with tens of metres-thick, organic-rich shales, both massive and laminated and characterized by scattered phosphate nodules, abundant macrofossils (mainly brachiopods) and occasionally marine reptile bones (e.g. Hurum, Roberts, Nakrem, Stenløkk, & Mørk, 2014). These laterally extensive shales are an important regional source rock (Senger et al., 2014) and represents a period of prolonged anoxic condition across the Barents Shelf during the Middle Triassic (e.g. Krajewski, 2013). The succession continues with the Early Carnian Tschermakfjellet Formation of the Kapp Toscana Group, which, together with the overlying and partly heteropic Middle Carnian De Geerdalen Formation, is inferred to represent the first major clastic (sand-rich) input in this part of the subsiding Barents Shelf (see Figure 1c,d). These formations partly correspond to the offshore Kobbe and Snadd equivalents (e.g. Anell, Faleide, & Braathen, 2016; Mørk et al., 1999; Nøttvedt et al., 1992; Vigran, Mangerud, Mørk, Worsley, & Hochuli, 2014), and are outstandingly exposed in the steep cliffs of southern Edgeøya (Figure 1c,e-g).

In summary, the broader depositional picture that emerges from these sedimentary successions is that of a large-scale delta system, built out over the northwestern coastal margin of an extended alluvial plain sourced from the Uralide orogen, and prograding into an anoxic, shallow and gentle relief shelf characterized by Middle Triassic platform deposits (e.g. Anell, Braathen, & Olaussen, 2014; Anell et al., 2016; Fleming et al., 2016; Haile et al., 2018; Klausen & Mørk, 2014; Klausen, Ryseth, Helland-Hansen, Gawthorpe, & Laursen, 2015; Mørk et al., 1999; Rød, Hynne, & Mørk, 2014). The maximum burial depth inferred for this succession has been calculated of several kilometres (Haile et al., 2018).

3 | STUDY AREAS AND METHODS

Growth faults are the product of syn-sedimentary activity and record progressive thin-skinned extension with associated localized sedimentation over variable time spans. They usually exhibit scale-invariant, listric geometries, with relatively steep fault planes close to the surface that progressively flatten with depth and sole-out into weak lithological intervals known as detachment zones or *décollements* (e.g. Bally, Bernoulli, Davis, & Montadert, 1981). Due to their geometry (see Figure 2a), listric faults are able to accommodate more horizontal extension by simple-shear than their planar counterparts, showing, for the same amount of displacement, larger horizontal displacements (i.e. heaves) and comparably smaller vertical displacements (i.e. throws; see e.g. Lohr, Krawczyk, Oncken, & Tanner, 2008).

FIGURE 1 Outline of the study area. (a) Geographic location of the Svalbard archipelago. (b) Simplified map of Svalbard with labelling of the major tectonic lineaments and location of Edgeøya (in black). (c) Schematic geological map of Edgeøya (redrawn from Osmundsen et al., 2014) with location of the study areas and representation of the main topographic lineaments (inset rose diagram). (d) Chronostratigraphic diagram showing the timing of syn-sedimentary faulting in the region and the main groups and formations cropping out on Edgeøya. (e–g) Overview of the study sites (e. Kvalpynten, f. Øhmanfjellet and g. Negerpynten) with labelling of the investigated faults, the cumulative listric and planar growth strike trends (inset rose diagrams)

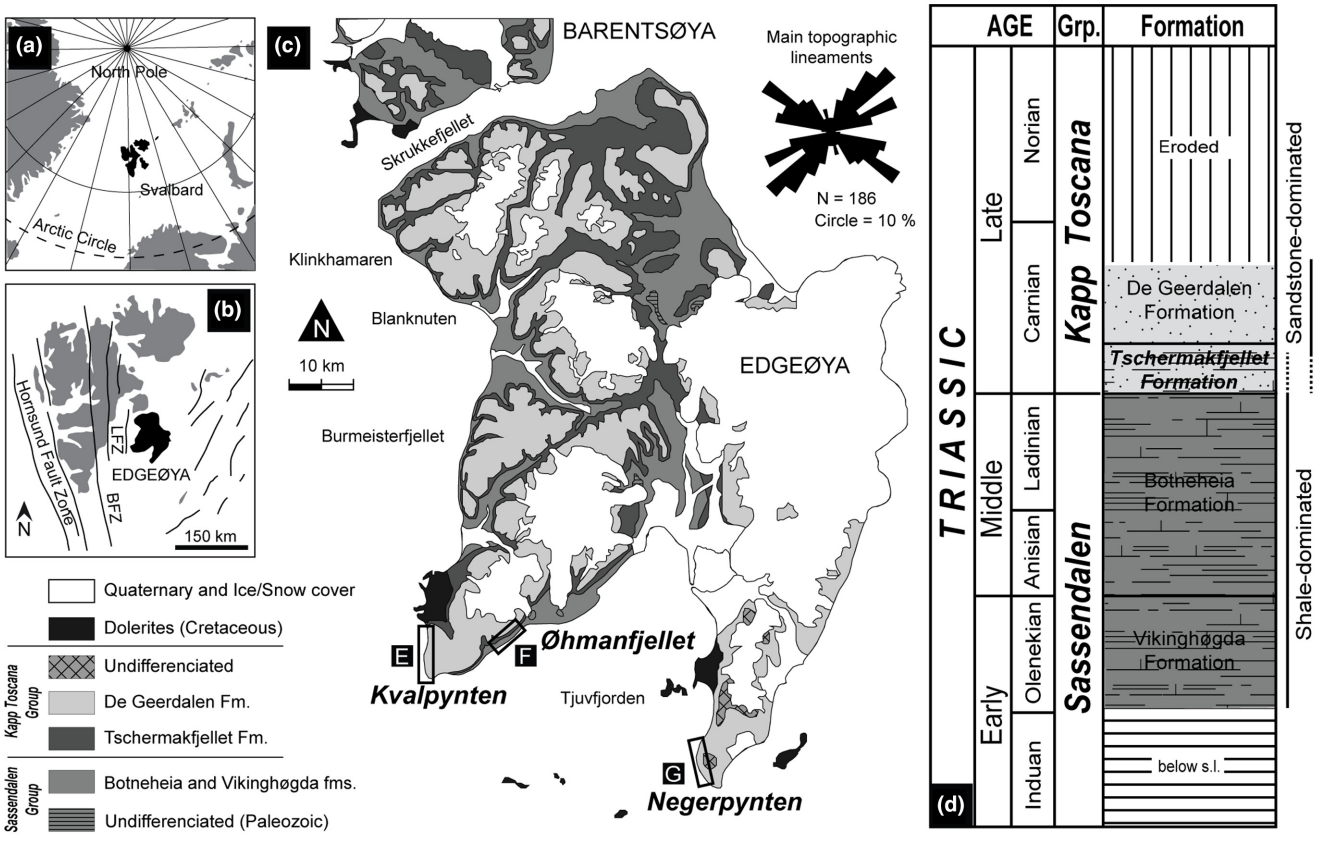
(a)
North Pole
Svalbard
Arctic Circle
(b)
Hornsund Fault Zone
LFZ
BFZ
EDGEØYA
N
150 km
(c)
BARENTSØYA
Skrukkefjellet
Klinkhamaren
Blanknuten
Burmeisterfjellet
EDGEØYA
N
10 km
Main topographic lineaments
N = 186
Circle = 10 %
E
F
Øhmanfjellet
Kvalpynten
Tjuvfjorden
G
Negerpynten
Quaternary and Ice/Snow cover
Dolerites (Cretaceous)
Kapp Toscana Group
Undifferenciated
De Geerdalen Fm.
Tschermakfjellet Fm.
Sassendalen Group
Botneheia and Vikinghøgda fms.
Undifferenciated (Paleozoic)
(d)
AGE
Grp.
Formation
TRIASSIC
Late
Middle
Early
Norian
Carnian
Ladinian
Anisian
Olenekian
Induan
Kapp Toscana
Sassendalen
Eroded
De Geerdalen Formation
Tschermakfjellet Formation
Botneheia Formation
Vikinghøgda Formation
below s.l.
Sandstone-dominated
Shale-dominated

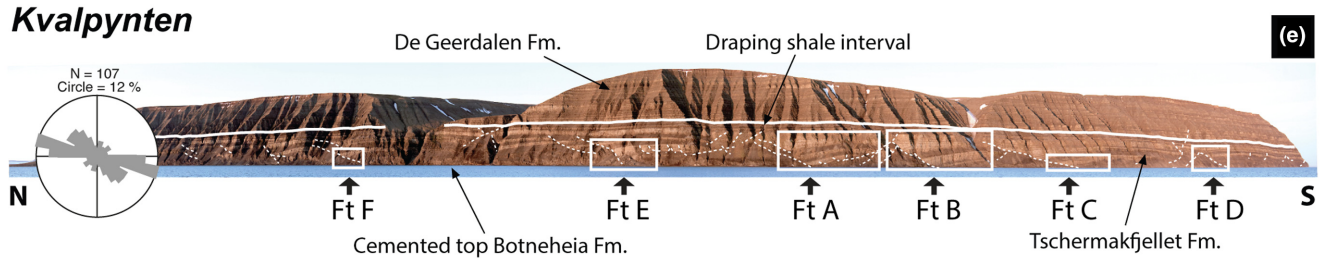
Kvalpynten
(e)
De Geerdalen Fm.
Draping shale interval
N = 107
Circle = 12 %
N
S
Ft F
Ft E
Ft A
Ft B
Ft C
Ft D
Cemented top Botneheia Fm.
Tschermakfjellet Fm.

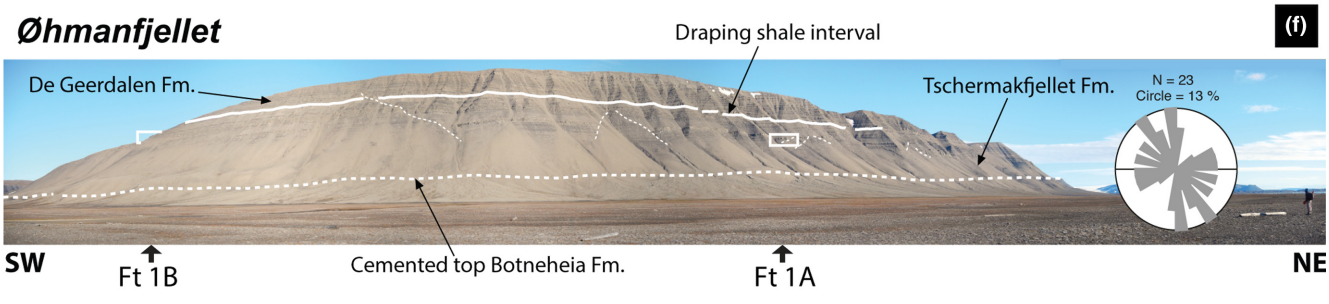
Øhmanfjellet
(f)
Draping shale interval
De Geerdalen Fm.
Tschermakfjellet Fm.
N = 23
Circle = 13 %
SW
NE
Ft 1B
Cemented top Botneheia Fm.
Ft 1A

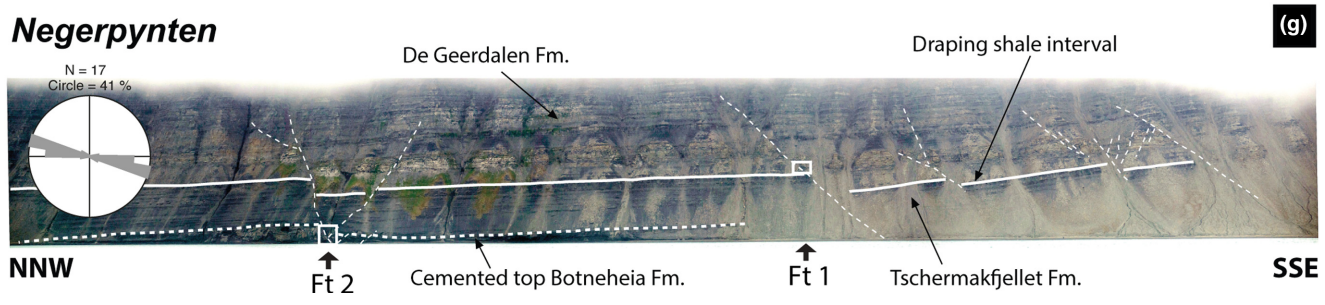
Negerpynten
(g)
De Geerdalen Fm.
Draping shale interval
N = 17
Circle = 41 %
NNW
SSE
Ft 2
Cemented top Botneheia Fm.
Ft 1
Tschermakfjellet Fm.

FIGURE 2 (a) conceptual representation of the investigated growth fault systems with indication of collected large-scale structural parameters (i.e. spacing, displacement, throw and heave) and the type of used markers (i.e. cut-off angle contacts, pregrowth and growth-wedges). (b) Interquartile box-plots of cumulative listric and planar growth faults' spacings (median values labelled). (c) Throw-heave-displacement plots for each investigated fault. (d) throw/heave ratio for each investigated fault. (e) Rectified slice of the photogrammetric 3D outcrop model of Kvalpynten with interpretation (f-g; normal and 6× vertically exaggerated line-drawings respectively) of the growth fault blocks and relative sedimentary wedges (in the inset, a simplified representation of the geometrical relationships among the three levels of fault hierarchies)

The study areas are located in the southern part of Edgeøya, where the laterally continuous, up to 500 m-high cliffs of Kvalpynten, Øhmanfjellet and Negerpynten (see locations in Figure 1c) provide detailed insights into the character of the Tschermakfjellet Formation growth fault systems and the over- and underlying De Geerdalen and Botneheia formations (see Figure 1e–g). These three sites represent an NNW-SSE transect stretching about 50 km in length across Tjuvfjorden bay, which provide a large-scale, three-dimensional perception of the stratigraphic interval containing the investigated growth-fault array.

Field data collection has been backed up by a photogrammetric 3D virtual outcrop model collected through ground-based (i.e. boat-mounted for a continuous shooting), georeferenced photo acquisition with combined high-resolution DSLR camera and differential GPS. The model has been interpreted analysed in LIME (http://virtualoutcrop.com/lime) to quantify large-scale (e.g. hundreds of metres) fault attributes, adapting the workflow described in Rittersbacher, Howell, and Buckley (2014): 1) horizontal spacing, 2) throw, 3) heave and 4) displacement (see Figure 2a). The principal offset marker used for these measurements, both in the field (where possible) and on the geomodel, is the cut-off line of lithologic contacts. Especially useful is the one between the fine-grained, early growth successions and the sandstone-dominated late-growth parts in the footwall sections (close to the fault tips), and relative counterparts in the hangingwall (see below), due to the clear colour contrast and lateral continuity on the large scale. Fine-tuning of these measurements has been performed by checking also the consistency of the geometrical relationships in the internal stratification of the sedimentary growth wedge and ground-truthing the information in the field. It is important to note that, due to the highly curvilinear attitude of the fault planes jeopardizing the consistency of the 3D measurements, the fault spacing has been taken as the horizontal 2D distance between two consecutive inflection points of the fault plane (i.e. where the listric fault plane sole out in the related detachment) marked by clear "shale cusps" instead of the actual perpendicular distance between two consecutive faults planes (see Figure 2a).

Approximately 35, 1:20 scale structural-stratigraphic logs were obtained in the coastal exposures of Kvalpynten, Øhmanfjellet and Negerpynten (see Figure 1e–g), to collect quantitative data on discrete fault elements and the overall structural architecture (i.e. apparent rock cohesion, lithology, sedimentary and tectonic structures and kinematic indicators, thickness/size of the fault elements) of eight listric and two planar growth faults at the outcrop scale (Figure 3a–c). For the mesoscale (centimetres to tens of metres) structural data acquisition, we follow the Fault Facies concept introduced by Braathen et al. (2009), in which the fault envelope consists of a varying number of discrete fault facies originating from the host rock and (re) organized spatially according to strain distribution and displacement gradients. Fault facies are thus related to size, geometry, internal structure, petrophysical properties and spatial distribution of fault structures, and can be hierarchically organized in architectural elements, hereafter defined by fault facies associations (FFA) and individual fault facies (IFF). These litho-structural units and their relationships define the basic elements of a conceptual fault zone or envelope (e.g. Caine, Evans, & Forster, 1996; Braathen et al., 2009), populated by a fault core, damage and mixing zones, in turn comprising lenses, smears and membranes of gouge, breccia) and shatter zones (e.g. Braathen, Osmundsen, & Gabrielsen, 2004.

As shown in Figure 3, for growth faults from A to E (Kvalpynten), and 1A (Øhmanfjellet), at least three correlated logs were recorded in the "proximal" (lower-displacement), "intermediate" and "distal" (higher-displacement) positions. For the remaining faults (i.e. fault 1B in Øhmanfjellet, and 1 and 2 in Negerpynten), due to the limited outcrop accessibility, structural stations (i.e. punctual and distributed measurements on a defined, laterally discontinuous area encompassing the favourable fault exposure) have been adopted instead.

Along with the structural-stratigraphic logging, systematic oriented sampling of the different fault facies and elements (from the pristine hanging wall and footwall country rock to the fault core) was conducted. Petrophysical and microstructural analyses have been performed on 42 samples to quantify porosity, pore size and density variations across fault zones, and to identify the microfabric, lithological changes and related deformation mechanisms.

A PoreMaster 33 porosimeter (Quantchrome Instruments) was used to measure porosity and pore size distribution by mercury-intrusion on unoriented samples, ca. 1 cm^3 in size. Before measurement, samples were dried at 40°C for 24 hr, and then ~1.5–2 g of material was analysed. The parameters

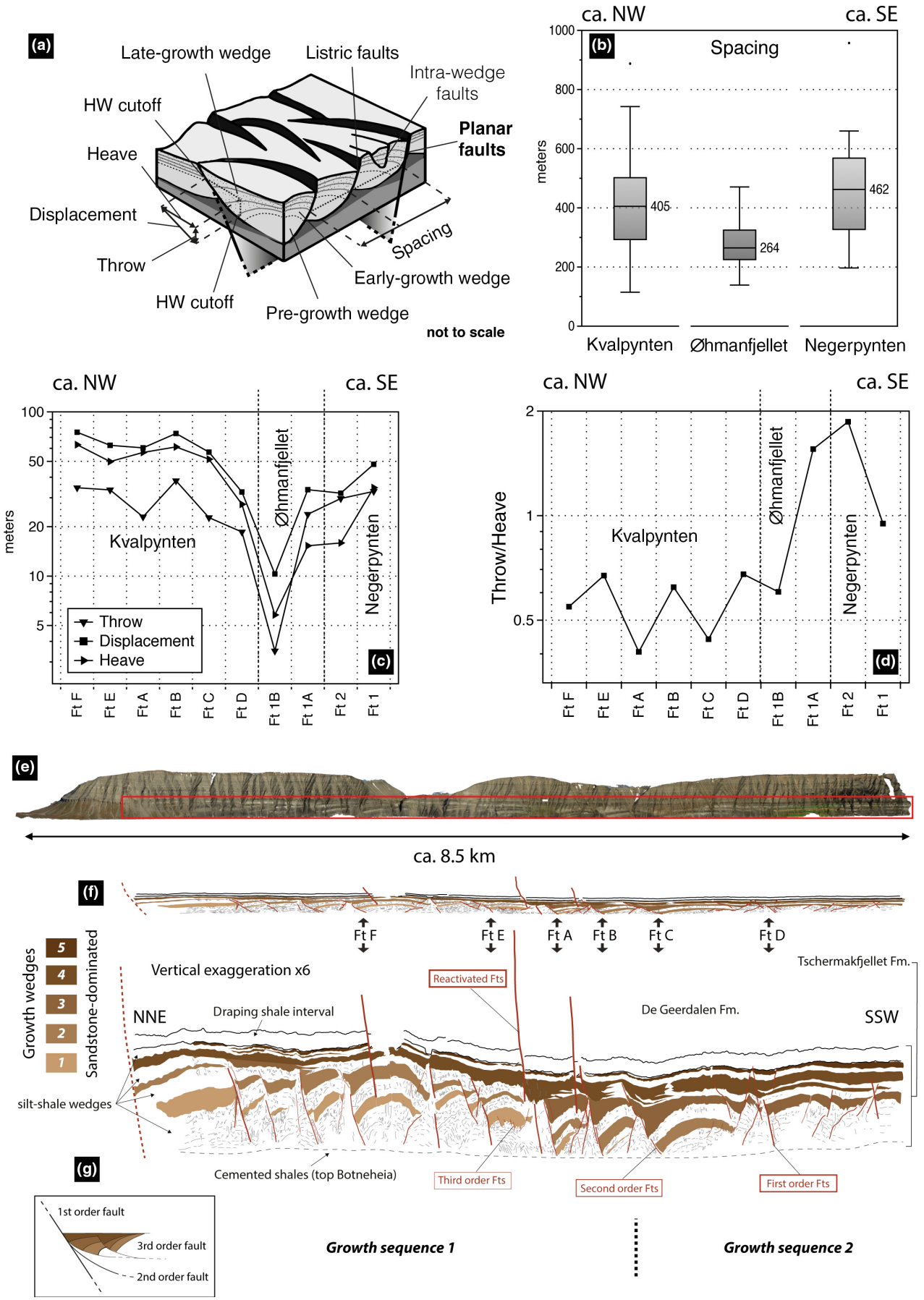
(a)
Late-growth wedge
Listric faults
Intra-wedge faults
HW cutoff
Planar faults
Heave
Displacement
Throw
Spacing
Early-growth wedge
HW cutoff
Pre-growth wedge
not to scale
ca. NW
ca. SE
(b)
Spacing
meters
1000
800
600
400
200
0
405
264
462
Kvalpynten
Øhmanfjellet
Negerpynten
ca. NW
ca. SE
(c)
meters
100
50
20
10
5
Kvalpynten
Øhmanfjellet
Negerpynten
Throw
Displacement
Heave
Ft F
Ft E
Ft A
Ft B
Ft C
Ft D
Ft 1B
Ft 1A
Ft 2
Ft 1
ca. NW
ca. SE
(d)
Throw/Heave
2
1
0.5
Kvalpynten
Øhmanfjellet
Negerpynten
Ft F
Ft E
Ft A
Ft B
Ft C
Ft D
Ft 1B
Ft 1A
Ft 2
Ft 1
(e)
ca. 8.5 km
(f)
Ft F
Ft E
Ft A
Ft B
Ft C
Ft D
Growth wedges
5
4
3
2
1
Sandstone-dominated
Vertical exaggeration x6
Reactivated Fts
Tschermakfjellet Fm.
NNE
Draping shale interval
De Geerdalen Fm.
SSW
silt-shale wedges
Cemented shales (top Botneheia)
Third order Fts
Second order Fts
First order Fts
(g)
1st order fault
3rd order fault
2nd order fault
Growth sequence 1
Growth sequence 2

used for measurements are as follows: sample cell is 1.0 × 3.0 cm, pressure range is 0.5–33000 psi, pore size range is 0.0064 to 950 μm, contact angle of mercury is 140 degrees, and surface tension of mercury is 0.48 N/m (480 dyn/cm). The volume of mercury penetrating into porous samples can be measured as a function of the applied hydraulic pressure. The obtained intrusion and extrusion curves were interpreted into pore size distributions in terms of the Washburn equation (Washburn, 1921), in which the applied hydraulic pressure P is related to the cross-sectional radius R of pore-throats accessible by the pressured mercury, together with two material-related, thermodynamic parameters: surface tension of mercury γ and its contact angle θ with the sample material involved (León Y León, 1998). Density measurements were performed with a Helium Pycnometer Ultrapic 1200e Quantachrome.

Optical microscopy observations in direct and polarized transmitted light were performed on oriented thin sections with a digital camera-equipped Zeiss AxioPlan 2 microscope. The same samples were then processed for SEM analyses with a vacuum evaporator JEOL JEE-4X, and backscatter electron images were produced using a Scanning Electron Microscope JEOL 6400, operating under high vacuum conditions (10–4 Pa) and equipped with Energy Dispersive X-Ray Microanalysis System (EDS) Oxford-INCA, and Si(Li) window-less detector.

4 | RESULTS

4.1 | Growth fault basin architectures and infills: baseline observations

A first regional interpretation of aerial photographs and digital elevation models of Edgeøya allowed the identification of two main regional structural trends (i.e. main topographic lineaments) striking NW-SE and NE-SW, which strongly influenced the overall geomorphology (e.g. linear valleys, fjords, hill-bridges and other linear features; see rose diagram in Figure 1c). These orientations are slightly to strongly oblique to the mean WNW-ESE (and subordinate NNW-SSE) strike of the investigated growth faults (see rose diagrams in Figure 1e–g).

Based on the outcrop-scale geometry and lateral-vertical continuity (e.g. hanging wall rollover occurrence, relationship with the lower detachment and upper draping units), a first rough distinction between listric and planar growth faults is recognized (as described in Osmundsen, Braathen, Rød, & Hynne, 2014). Listric faults concentrate in SW Edgeøya around Kvalpynten (Figure 1c) and planar faults dominate around the SE (i.e. Negerpynten; see Figure 1). The listric faults are characterized by 1) a generalized ductile-plastic style of deformation (i.e. "soft"), 2) clearly exposed scoop-shaped, concave-upwards geometries at the outcrop scale and 3) well-developed rollover anticlines, while planar faults generally lack such features. The incremental displacement achieved on planar faults appear to sometimes rotate the synthetic listric faults arrays located in their hanging wall blocks, suggesting a deep-rooted listric origin for at least some of them. The spatial variation in the fault strikes for the different localities (see rose diagrams in Figure 1e–g), can be attributed to the partly curvilinear attitude of some of the single listric growth fault strands and/or and how exposures intersect the faults.

The combined structural parameters obtained for both planar and listric faults in the Tschermakfjellet interval (see Figure 2a) show a similar range of spacing across the investigated areas, with comparable median values for Kvalpynten and Negerpynten, and lower numbers in the Øhmanfjellet fault array (see Figure 2b). The same pattern appears in terms of relative values of throw, heave and displacement, with absolute lower values for Øhmanfjellet area. Notably, a switch in the throw and heave values seems to mark a transition from more listric-like to more planar-like faults from the NW towards the SE (see Figure 2c). This tendency is also testified and strengthened if these values are normalized, as shown by the trend of throw/heave ratios (see Figure 2d).

A detailed 3D outcrop model interpretation of the faults and fault blocks of the Kvalpynten area (Figure 2e–g) allowed the recognition of at least two major growth fault sequences comprising four to five fill cycles (i.e. coarsening upward from shale to sandstone parasequences) with well-developed sandstone-dominated, late-growth wedges in the upper part (see Figure 2e–g). On the basis of the geo-model and *in situ* observations, three orders of faults appear to occur, hereby classified from first to third order. Their ranking based on the following criteria: 1) the associated sole out detachment, 2) the lateral-vertical continuity, 3) the reciprocal position and 4) outcrop-scale extension (Table 1). The first-order faults extend below sea level and therefore the associated detachment is not exposed, appearing truly planar and through-going. The second-order faults zones share a basal detachment interval located atop the well-cemented uppermost Botneheia Formation and show clear listric geometries. The third-order listric faults are usually synthetic to the second-order ones and located in their hanging wall blocks, with their detachment level located near the base of the sandstone-dominated, coarsening upward parasequences (i.e. late-growth wedges) of the Tschermakfjellet. In particular, for the more symmetric grabens, a significantly larger amount of third-order faults antithetic to the first-order one occur with respect to the less symmetric ones (see Figure 2g). All the three types of faults were top-bounded by a sealing, laterally continuous shale interval that cap and drapes the growth faulting interval (see Figure 2f). Few later faults in the De Geerdalen

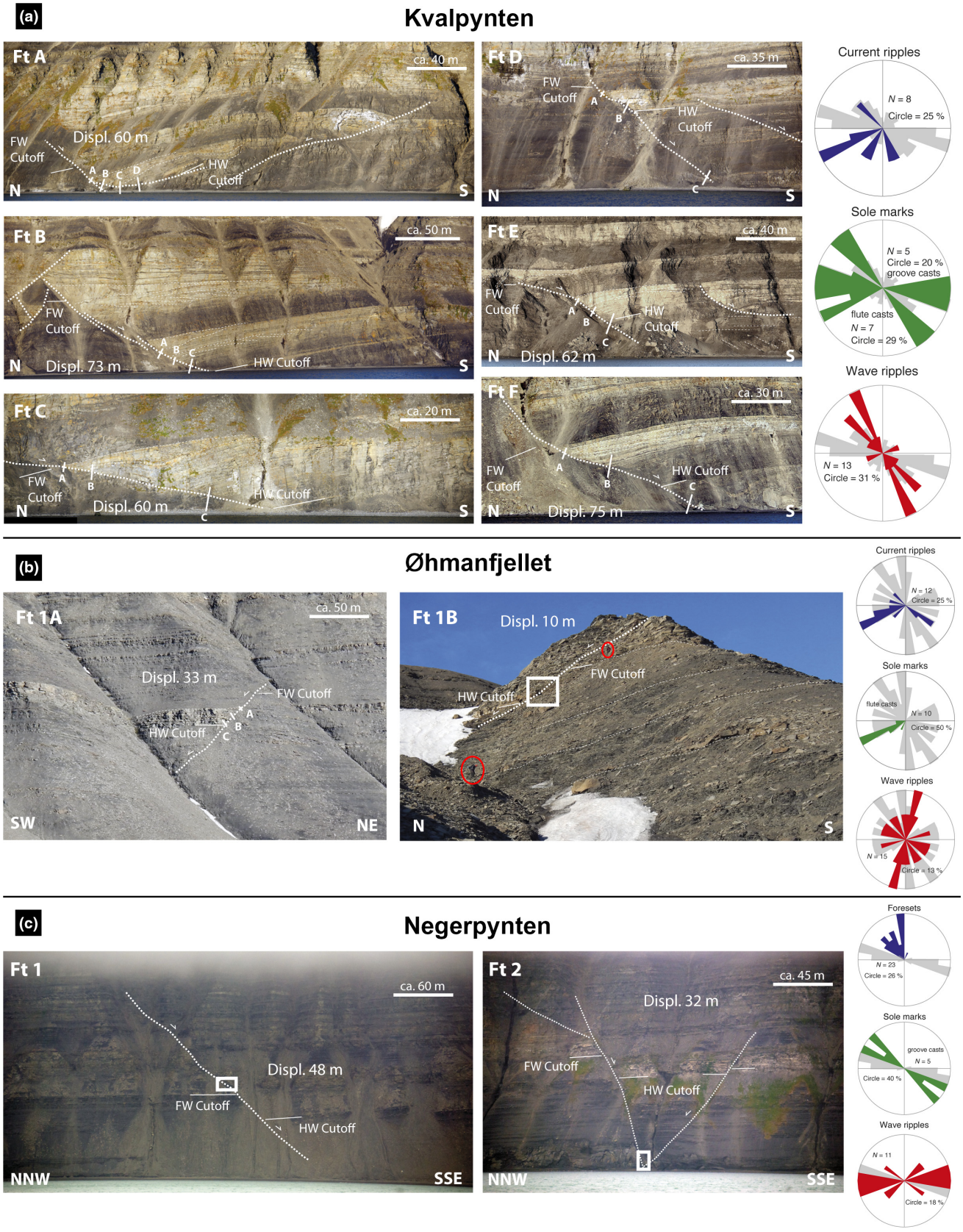

FIGURE 3 Overview of the analysed faults, with locations of the collected fault logs and structural stations, for each study area: (a) Kvalpynten, (b) Øhmanfjellet (persons for scale in Ft b), and (c) Negerpynten. For each study area, rose diagrams summarizing the local palaeocurrent data (current ripples/forests, groove and flute marks, and wave ripple crests) are shown along with the cumulative listric and planar growth fault strike (see Figure 1e–g) in the background (in gray)

TABLE 1 Diagnostic criteria used for fault classification

Fault	Detachment	Lateral-vertical continuity	Reciprocal position	Fault length/height
1st order	Not exposed (below s.l.)	Planar	-	Through-going
2nd order	Top Botneheia Fm.	Listric	HW of 1st order	10-100s metres
3rd order	Within Tschermakfjellet Fm.	Listric	HW of 2nd order	1-10s of metres

cut downward through the draping shale and appear to exploit the favourably oriented first- and second-order fault segments to reach and sometimes cut across the top Botneheia detachment, with complex interlinking relationships across the growth faulting interval (see Figure 2g).

The sandstone-dominated, growth fault wedges developed in the hangingwall of first- to second-order faults comprise thickening- and coarsening-upward successions, represented from the base upwards, of (1) laminated mudstones-siltstones with thin-bedded fine-grained sandstones interpreted as prodelta deposits, which become progressively punctuated by (2) graded beds with planar and ripple laminations, sometimes characterized by erosive bases, sharp tops, hummocky-type cross stratification and "pinch-and-swell" trends, and, towards the top, (3) heterolithic interbedded sand/siltstones with wavy-, lenticular- and flaser- bedding, passing upward into cross-bedded (planar- and through-), very fine- to fine-grained sandstones arranged in metres- to tens of metres thick and tens to hundreds of metres-wide sedimentary wedges. In this stratigraphic framework, the laminated mudstones-siltstones that characterize the lower part of the hangingwall represent the early growth stages passing into upper syn-growth sandstone-rich intervals, as also testified by the lateral stratigraphic wedging marked by rapid thickness changes and, in places, biunded by progressive (laterally fanning and converging) unconformities.

The footwall sections are entirely represented by pregrowth, laminated mudstones-siltstones, with thin overlying early growth sequences, in places showing stratigraphic wedging. In these FW sections, bedding rotations are sometimes observed as well within folded and intensely deformed intervals, not always clearly distinguishable due to the low lithological contrast. These pregrowth FW sediments are sometimes characterized by bedding-parallel and unconformable surfaces with high erosional outcrop relief (i.e. standing out from the exposure). They show characteristics similar to the well-cemented top Botneheia Formation), and usually mark the lower contact onto which thin (up to few metres-thick), highly erosive FW sandstones wedges that rapidly pinch out laterally, away from the fault (see Figure 2e–g and Figure 3). Due to these characteristics, these surfaces are used as FW cut-off markers (see Figure 2a).

At Kvalpynten, the transition between the Tschermakfjellet and De Geerdalen formations is defined by a conformable, laterally extensive interval of draping dark shales, which mark the upper boundary of the growth fault system, with only few later, reactivated fault zones cutting across and displacing this interval and the overburden. On the other hand, at Negerpynten most of the dominant, planar faults cut up high into the De Geerdalen Formation (see Figure 2e–g). This latter Formation locally consists of fine- to medium-grained sandstone and heterolithic bed-sets, characterized by an upward increase in organic content (i.e. plant fragments) and (marine to continental) bioturbation, and by the occurrence of condensed and red-bed intervals towards the top. Channelized bodies comprising amalgamated sandstone bed-sets with through-cross laminations punctuate the overall succession.

Complementary palaeo-current measurements collected along with stratigraphic-structural logging of fault blocks show significant variations among the reference areas, with primary sedimentary flows recorded by sole marks (e.g. groove and flute casts) suggesting NW to SW directions, secondary flows recorded by traction-plus-fallout structures (e.g. cm- to m-sized forests and asymmetric ripples) with

FIGURE 4 Fault architectural elements (AE) defined by fault facies associations (FFA), and single fault facies (SFF) in the framework of a conceptual fault envelope. (a) Conceptual representation of the investigated fault profile with indication of the main structural features and AEs and SFFs. Inspired, modified and updated from Loveless et al. (2011). (b) Overview of the upper part Fault d with labelling of the main AEs (see text). (c) Examples of the identified FFAs, with indication of their associated SFFs (bold italic white labels in pictures) and associated AEs (see text and Table 1 for details). (d) Detail of the lower part of Fault D (close to the main detachment) showing shale-shale juxtaposition. Note the occurrence of detached lenses of FWMZ and HWMZ. (e–h) Brittle-ductile structures, kinematic indicators, and CZ features from Fault b (e), Fault c (f), Fault f (g) and Fault d (h). Note in E the occurrence of preserved (inherited) ductile (e.g. SCC'-type structures) bounded, reworked and crosscut by brittle structures (e.g. microduplex, striated lithons, discontinuous shear surfaces) in the fault gouge. A feature observed in all the examples is the systematic occurrence of high degree of oxidation, due to localized increase content of Fe-sulphides (pyrite) in the soft sediment sheared part of the inner HWDZ, HWMZ and CZ. The same oxidation pattern is observed in fault gouges, both in sand-shale and shale-shale juxtapositions (see F and G, and H respectively). Person, hammer, GPS or gloved/bare finger for scale

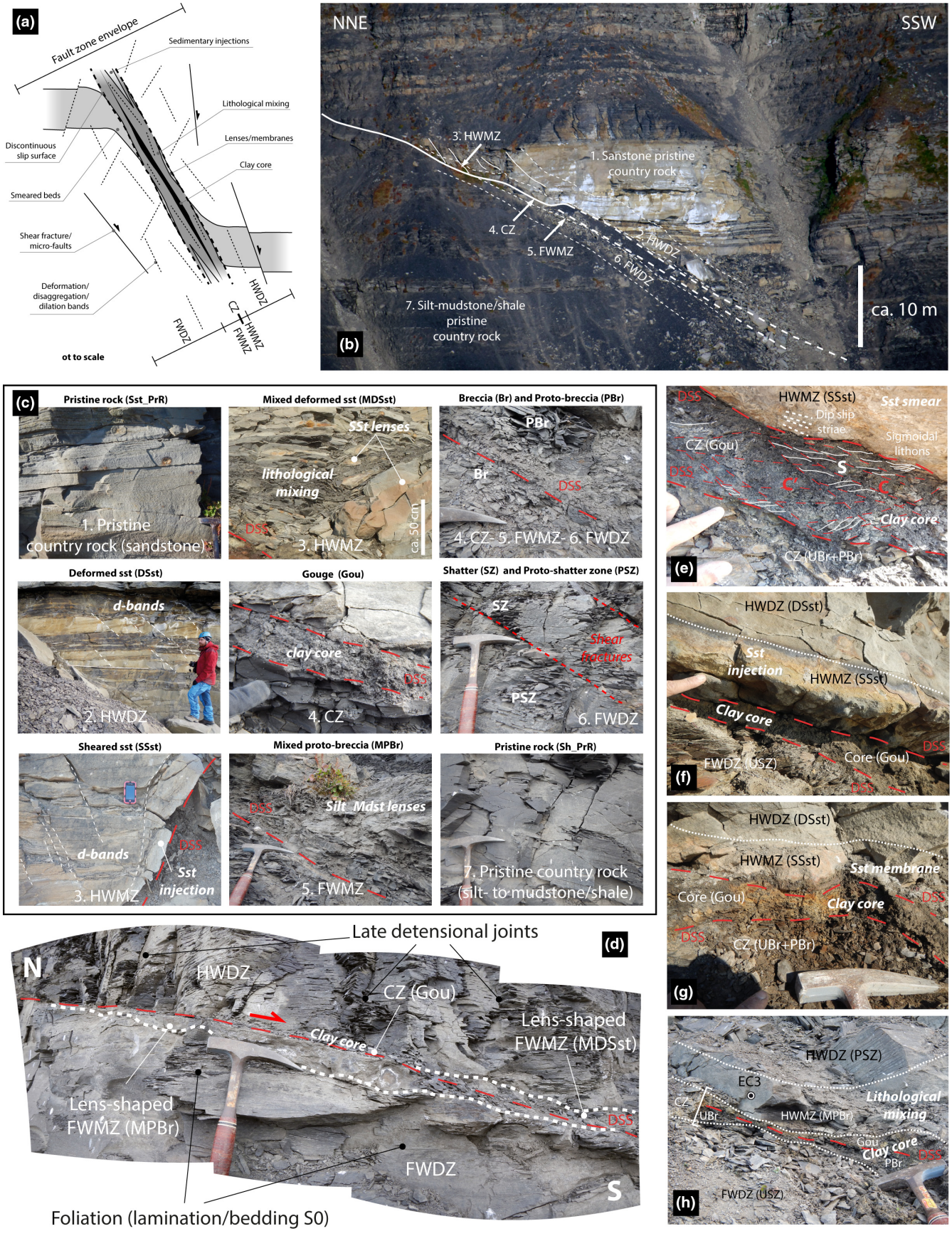
(a)
Fault zone envelope
Sedimentary injections
Lithological mixing
Lenses/membranes
Clay core
Discontinuous slip surface
Smeared beds
Shear fracture/ micro-faults
Deformation/ disaggregation/ dilation bands
HWDZ
CZ
HWMZ
FWMZ
FWDZ
ot to scale
NNE
SSW
3. HWMZ
1. Sanstone pristine country rock
4. CZ
5. FWMZ
2. HWDZ
6. FWDZ
7. Silt-mudstone/shale pristine country rock
ca. 10 m
(b)
(c)
Pristine rock (Sst_PrR)
1. Pristine country rock (sandstone)
Mixed deformed sst (MDSst)
SSt lenses
lithological mixing
DSS
3. HWMZ
ca. 50 cm
Breccia (Br) and Proto-breccia (PBr)
PBr
Br
DSS
4. CZ- 5. FWMZ- 6. FWDZ
Deformed sst (DSst)
d-bands
2. HWDZ
Gouge (Gou)
clay core
DSS
4. CZ
Shatter (SZ) and Proto-shatter zone (PSZ)
SZ
Shear fractures
PSZ
6. FWDZ
Sheared sst (SSst)
d-bands
DSS
Sst injection
3. HWMZ
Mixed proto-breccia (MPBr)
DSS
Silt_Mdst lenses
5. FWMZ
Pristine rock (Sh_PrR)
7. Pristine country rock (silt- to mudstone/shale)
(d)
N
Late detensional joints
HWDZ
CZ (Gou)
Clay core
Lens-shaped FWMZ (MDSst)
Lens-shaped FWMZ (MPBr)
DSS
FWDZ
S
Foliation (lamination/bedding S0)
DSS
HWMZ (SSst)
Sst smear
Dip slip striae
Sigmoidal lithons
CZ (Gou)
S
C'
C
Clay core
CZ (UBr+PBr)
(e)
HWDZ (DSst)
Sst injection
HWMZ (SSst)
Clay core
FWDZ (USZ)
Core (Gou)
DSS
(f)
HWDZ (DSst)
HWMZ (SSst)
Sst membrane
Core (Gou)
Clay core
DSS
CZ (UBr+PBr)
(g)
HWDZ (PSZ)
EC3
CZ
UBr
HWMZ (MPBr)
Lithological mixing
Gou
Clay core
PBr
DSS
FWDZ (USZ)
(h)

similar orientations but wider spread, and tidal-wave interference structures (e.g. symmetric ripples) providing directions approximately perpendicular to the former (from ca. E-W in Negerpynten, to NNE-SSW and NNW-SSE in Tjuvfjorden and Kvalpynten respectively; see rose diagrams in Figure 3a–b).

4.2 | Growth fault zones, elements and litho-structural facies

Fault zone architecture has been herein described according to the classic definition proposed in the literature for mesoscale brittle faults: a deformed volume of rock that accommodates movement between two blocks, commonly comprising an inner fault core which accommodate most of the displacement (and include the principal slip surface) surrounded by a footwall-hanging wall damage zones (see e.g. Braathen et al., 2009; Caine et al., 1996; Sibson, 1977). Complementary studies extended this model to fault envelopes in poorly lithified sediments, introducing the mixed (or mixing) zone as a third architectural element that separate fault core from damage zone. The mixed zone consists of variably deformed, entrained and attenuated beds forming continuous smears along the fault trace, resulting in a largely homogenized zone with lithological mixing down to the grain scale (see e.g. Balsamo, Bezerra, Vieira, & Storti, 2013; Bense & Person, 2006; Braathen et al., 2013; Heynekamp et al., 1999; Loveless et al., 2011; Mozley & Goodwin, 1995; Rawling & Goodwin, 2003, 2006).

According to this general framework, we subdivide the investigated fault envelopes into fault architectural elements (AE; Figure 4a,b): 1) hanging wall damage zone (HWDZ), 2) hanging wall mixing zone (HWMZ), 3) fault core zone (CZ), 4) footwall mixing zone (FWMZ) and 5) footwall damage zone (FWDZ). These AEs are in turn made up by specific litho-structural, fault facies associations (FFA), distinguished on the basis of the dominant lithologies and single fault facies (SFF), as shown in Figure 4c–h and listed in Table 2. Their relative abundance and mutual relationships differ between the third- and first-order faults, which can be considered as purely listric (soft) and planar (hard) end-members respectively.

In the listric faults' hanging wall, the pristine, relatively undeformed, sandstone country rock (Sst_PrR; Figure 4c), is progressively plastically deformed, from lower strain conditions in the HWDZ (DSst; Figure 4c), to higher strain conditions involving localized mesoscale lithological mixing in the HWMZ (MDsst; Figure 4c), and eventually becoming more intensively deformed close to the contact with the CZ (SSst; Figure 4c). Such elements are characterized by the combined occurrence of disaggregation (dilation/compaction), deformation and phyllosilicate bands (e.g. Fossen, 2010), hydroplastic intrafolial folds and boudinage-related products, testifying to an increasing intensity of deformation towards the fault core (see below). In the planar fault zones, the HWMZ is usually missing, sometimes appearing as remnants within the HWDZ and/or incorporated as lenses into the CZ.

Disregarding later overprinting by brittle deformation structures (e.g. tensional and shear fractures, cliff-side joints), which usually rework inherited discontinuities (e.g. deformation disaggregation and phyllosilicate bands), the CZ of listric faults comprise one or more discontinuous principal slip planes with crude pseudostriations. These slip surfaces bound membranes of plastically mixed sand and/or clay, and an assemblage of elongated elements (e.g. detached smears, membranes, lenses, etc.) with their long axes trending roughly parallel to the fault trace. These latter elements are enclosed in, or associated with, gouge levels (Gou; Figure 4c). In contrast, in planar faults, one or more striated principal slip surfaces are commonly observed to bound relatively continuous gouge and breccia membranes.

The footwall sections of listric faults start with a lithologically mixed protobreccia (MPBr; Figure 4c) at a transition defining or within the FWMZ, with a relatively constant lenticular trend and thus locally missing due to lateral pinch-outs. In the inner FWDZ, the progressive deformation in a dominantly semibrittle regime leads to significant loss in cohesion, resulting in a protobreccia (PrB; Figure 4c) that eventually grades into noncohesive breccia zones (Br; Figure 4c) in close proximity and within the CZ. The outer FWDZ is made up by slightly to pervasively fractured mud rocks, termed, respectively, as proto-shattered zones (PSZ) to shattered zones (SZ). These zones, characterized by inwards decreased spacing of structural discontinuities and fractures (Figure 4c), progressively involve the undeformed background lithology (i.e. pristine country rock) of laminated to massive silty shales (Sh_PrR; Figure 4c). As for the hangingwall (HW), in planar faults the FWDZ is wider (up to tens of metres) and characterized by pervasive fracturing of the preexisting fabric, whereas the FWMZ (and sometimes the HWMZ) is usually preserved as lenses and membranes of plastically deformed footwall (FW) lithologies, juxtaposed to and within the CZ (Figure 4d–h). These litho-structural elements are cut and bounded by discontinuous slip surfaces, tensile and shear fractures and disaggregation-deformation and phyllosilicate bands (e.g. Fossen, Schulz, Shipton, & Mair, 2007; Torabi, Fossen, & Braathen, 2013), as well as hydroplastic structures (e.g. Maher, Ogata, & Braathen, 2017).

Sedimentary injection-type structures occur mainly within the inner HWMZ (Figure 5a,b) and are commonly preserved along antithetic and synthetic, subsidiary normal faults internal to the growth fault block. Smearing of sand-rich sediments along the fault traces occurs in many cases

TABLE 2 Description and interpretation of the single fault facies (SFF) as illustrated in Figure 4c

Single fault facies (SFF)	Description	Lithologies	Structures	Interpretation
Undeformed sandstone (Sst_PrR)	Pristine, relatively undeformed, sandstone	Fine to medium sandstones with interbedded siltstones-mudstones	Grading, sedimentary structures preserved	Country rock "protolith"
Deformed sandstone (DSst)	Massive to crudely banded sandstone with arrays of structural discontinuities	Fine to medium sandstones with interbedded siltstones-mudstones	Massive, unsorted texture with deformation and disaggegregation bands; isolated framboidal pyrite nodules; hydroplastic intrafolial folds; boudinage-related products	Plastically deformed country rock at low strain conditions
Sheared sandstone (SSst)	Massive sandstone	Fine to medium sandstones with interbedded siltstones-mudstones	Massive, unsorted texture with pervasive shear-related structures; continuous pyrite cementation	Plastically deformed country rock at high strain conditions
Mixed deformed sandstone (MDSst)	Massive to brecciated sandstone -mudstone assemblage	Fine to medium sandstones with interbedded siltstones-mudstones and mudstones	Massive, unsorted and finer grained texture with pervasive shear-related structures; lithological mixing; continuous pyrite cementation; hydroplastic intrafolial folds; boudinage-related products	Plastically deformed and mixed sandstone-mudstone elements
Gouge (Gou)	Fine grained, unconsolidated material with scattered angular country rock microclasts	Fine to very fine, uncemented, swelling siltstones-mudstones	Usually massive with sometimes scaly fabric, SCC'-structures, microduplexes, striated sigmoidal lithons	Brittle crushing and comminution of plastically deformed and mixed mudstone elements
Mixed breccia (MBr)	Fine grained, consolidated material with angular country rock fragments	Fine to very fine cemented siltstones-mudstones mixed with sandstone levels	Relatively constant lenticular trend; caly fabric, SCC'-structures, microduplexes, striated sigmoidal lithons	Plastic mixing of brittle mudstones and ductile silt-sandstones
Breccia (Br)	Noncohesive assemblage of angular silt-mudstone elements	Fine to very fine cemented siltstones-mudstones	Breccia texture, sometimes with localized scaly fabric, SCC'-structures, microduplexes, striated sigmoidal lithons	Pervasive fracturing of plastically deformed, indurated mudstone elements
Protobreccia (PBr)	Poorly cohersive assemblage of fracture-bounded sitl-mudstone elements	Fine to very fine cemented siltstones-mudstones	Very closely spaced nonsystematic pervasive fracturing (tensional and shearing)	Progressive deformation in a dominantly ductile-brittle regime
Shatter zone (SZ)	Cohesive and pervasively fractured silt-mudstone	Fine to very fine cemented siltstones-mudstones	Closely spaced nonsystematic pervasive fracturing (tensional and shearing)	Progressive deformation in a dominantly semibrittle regime
Protoshatter zone (PSZ)	Cohesive and relatively fractured silt-mudstone	Fine to very fine cemented siltstones-mudstones	Spaced nonsystematic pervasive fracturing (tensional and shearing)	Progressive deformation in a dominantly brittle regime
Undeformed shale (Sh_PrR)	Pristine, relatively undeformed, silt-mudstone (shale)	Fine to very fine cemented siltstones-mudstones	Sedimentary structures and fossils preserved	Country rock "protolith"

(Figure 5c), together with hydroplastic drag folding of the wall rock beds, sometimes with rotation and complete detachment of the fold hinges (Figure 5d,e). Other associated structures recording plastic-ductile stages of deformation, are symmetric and asymmetric pinch-and-swell structures and boudinage, mostly preserved within

FIGURE 5 Soft-sediment deformation, liquidization and hydroplastic features. (a) Example of sandy sedimentary injections along fault zone (Fault b). In this case the up- and down-going clastic wedges merge in the middle of the picture (see b). Circled person for scale. (b) Detail of B showing the sedimentary injections interacting. Note the increasing abundance of "clay chips" ripped up from the shale HW interbeds in the down-going injection, and the increasing oxidation towards the CZ in the up-going one. The locations of two sampling points are also shown (see DR 2). Camera lens cap for scale (ca. 7 cm in diameter). (c) Softsediment (hydroplastic) striations-lineations at HWMZ-CZ boundary (Fault 1a) with relative stereoplot (dotted circle is the main fault trace, solid circles are the shear surfaces, dots represent azimuth and plunge of striations-lineations). Field notebook for scale (ca. 20 cm long). (d) Hydroplastic folding in the inner part of FWMZ (Fault d). Gloved finger for scale. (e) Soft-sediment, detached and rotated sigma-shaped, sandstone lens in the third-order detachment zones. Note the high degree of incipient lithologic mixing. Circled camera lens cap for scale (ca. 7 cm in diameter). (f) Array of normal, soft-sediment microfaults (deformation-disaggregation bands) in HWDZ (Fault d). Camera lens cap for scale (ca. 7 cm in diameter). (g) Thin section from F showing one of these deformation-disaggregation bands (mm-displacement). (h) Detail of g under optical microscope. Note the dragging of laminae and the repacking/rearrangement and preferential alignment of grains without breakage. (i) Hydroplastic, reverse microfault zone in the third-order detachment zones. (j) Thin section from I showing a deformation-disaggregation bands (mm-displacement) comprising the reverse microfault zone. (k) Detail of j under optical microscope showing the preferential alignment of grains and platy minerals along a narrow shear zone. No syn-deformation cracking nor recrystallization are observed

the sandstone-dominated HWMZ. At the microscale (see below for a detailed discussion), the most representative structures are conjugate disaggregation-deformation bands characterized by mixed shear dilation-compaction in the sandstone-dominated HW (Figure 5f–h), and disaggregation-phyllosilicate bands and hydroplastic, intrafolial microfolds within the finer grained FWMZ (Figure 5i–k). Later, pervasive shear and tensile fracturing appears to be formed by reworking/reactivation of these primary (early postdepositional) structural features, which are preserved, for instance within structurally bounded lithons in CZs (see Figure 4e).

Notably, cone-in-cone (CIC) and beef (BF) carbonate veins arranged in lens-shaped aggregates ornament growth fault footwalls and detachment zones, and especially the low-angle shear zones at the top Botneheia (Figure 6a), as described in Maher et al. (2017). These features, arranged parallel to bedding and fault surfaces, are cm-thick, asymmetric, antitaxial tensile vein assemblages that enucleate from planar structural discontinuities (e.g. microcracks, disaggregation-phyllosilicate bands, fossil shell debris), permeating the silty-shaly country rock (Figure 6b–d). In the investigated sites, the CIC/BF assemblages are progressively deformed according to their position within the fault envelope, eventually recognizable in the CZ as isoclinally folded and fragmented lenses (Figure 6e–g). CIC lenses are also observed to be passively folded within ductile shear zones in the shaly FW, at fault tips and within the associated detachment zones, and within low-angle shear zones, as depicted in Figure 6a and 6h (see section 4.4 for further discussion).

Simple shear-related structures (e.g. SC-type structures), small-scale (cm- to dm-sized) duplexes and conjugate Riedel shears are widespread in the CZs. They indicate a shear sense compatible with the normal movement, consistent with striations characterizing the anastomosing and discontinuous slip surfaces (see Figure 4e–h). In this framework, the SC-type structures are ascribed to a plastic style of deformation transitioning towards a more brittle style along with duplexing and Riedel shear development. These latter structures appear developed at the expense of structural discontinuities formed in the earlier phases of ductile/plastic deformation, such as SC-type structures and conjugate arrays of deformation disaggregation bands, which a mechanical anisotropy prone to brittle reactivation.

Of particular note is the systematic occurrence of oxidation banding in the inner HWMZ and HWDZ (i.e. SSst) and oxidized gouge in CZ (see Figure 4e–h). These oxidation patterns derive from alteration of Fe-sulphide (i.e., pyrite), locally concentrated in the form of dispersed, discrete framboidal nodules and/or intergranular cement intervals. They trend parallel to the discontinuous shear surfaces characterizing subsidiary and principal fault zones.

The overall increasing deformation pattern from the outer to the inner FW is highlighted by an overall decrease in cohesion of the silty-shale lithologies, clearly recognizable from the erosional profile and semiquantitatively represented in form of fault logs (e.g. shown in Figure 7a; complete database in DR1). The lateral-vertical geometric relationships and spatial arrangement of the AEs, subdivided for each FFA, are summarized in Figure 7b. At mesoscale (i.e. cm- to tens of m-sized), with the exception of the mixing zones, fault architectural element thickness increases with increasing displacement, consistent with their widening with time. The HW architectural elements usually follow this general trend, apart from exceptions within the HWMZ and FWMZ, such as downward wedging sand dykes, and lens-shaped, pinch-and-swell arrangements of the plastically formed material (i.e. faults B and 1A respectively; see Figure 7b).

The two pure planar faults 1 and 2, characterized by sand-shale and shale-shale juxtaposition relationships, respectively, are taken as representative of the end-member brittle faults (1st order) for comparison (Figure 8). In both cases, the overall fault envelope is that of a classical normal fault, with well-developed core and damage zones

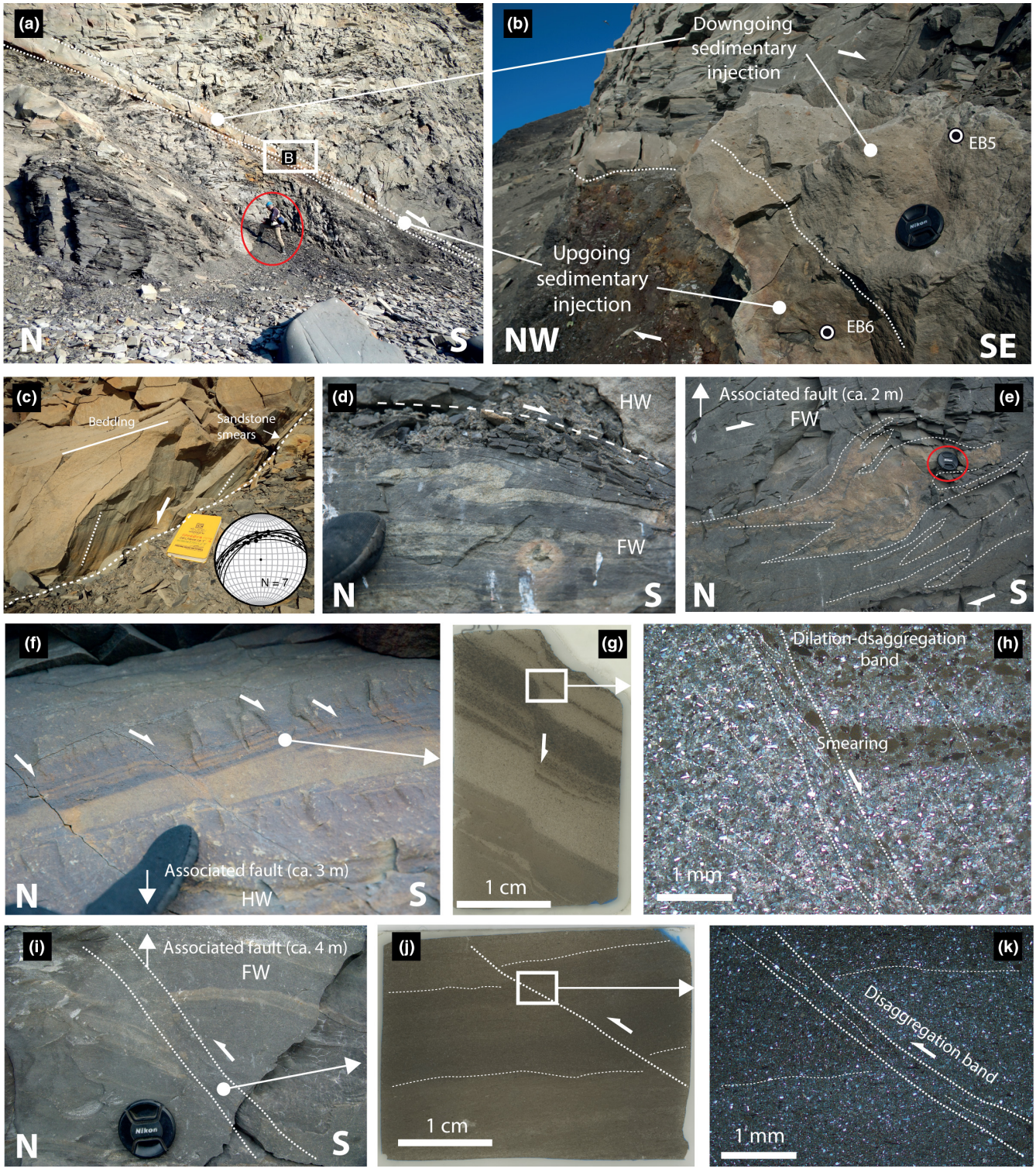

(Figure 8a,d), and without evidence of mixed zones. In these cases, the dominance of brittle deformation structures is evidenced by the occurrence of continuous slip surfaces with striations, bounding isolating sigmoidal lithons (Figure 8c), shale gouge membranes and CZ (Figure 8e). These are in turn characterized by microduplex and a general anastomosing patterns of shear surfaces, resembling in places a spaced scaly fabric (Figure 8e,f), which likely rework previous structures inherited from previous deformation phases (e.g. SC-type structures). Notably, detached FWMZ and HWMZ lenses, CIC veins and remnants of sedimentary injections-type structures are in places preserved in the HW and FW (see Figure 8b), and as lenses within the CZ.

FIGURE 6 Location and appearance of CIC/BF aggregates. (a) Overview of a shear zone belonging to the second-order detachment, showing HW and FW drag folds and internal occurrences of lenses and detached CIC/BF aggregates (white arrows). Person for scale. (b) Appearance of one of these CIC/BF aggregates (location in a). Camera lens cap for scale (ca. 7 cm in diameter). (c) Thin section from b showing a CIC vein. (d) Detail of c under optical microscope showing the V-shaped, fibrous growth of calcite nests from a common point, and surrounded by entrapped fine-grained sediments (for a detailed description of these mineral growths see Maher et al., 2017). (e) Lower part of Fault a, few metres above the associated second-order detachment, showing staked and folded sandstone lenses, represented by detached and disarticulated sedimentary injections, in the FWMZ, and in situ metre-sized CIC/BF aggregate lenses in the FWDZ, subparallel to the fault trace. (f) Lower part of Fault f, few metres above the associated second-order detachment, showing a detached lens of FWDZ with CIC/BF veins. Hammer for scale. (g) Detail of F showing drag folding of both laminae and CIC veins. Finger tip for scale. (h) Detail of a shear zone in a second-order detachment showing detached CIC/BF aggregates sheared into rootless, isoclinal folds and sigma-shaped lenses

4.3 | Microstructures and petrophysical attributes

The different architectural elements show changes in microfabric evolution, intensity and linear frequency of (micro) structures, with distinct litho-structural control on bulk pore size, in both vertical (i.e. across fault) and lateral (i.e. along fault) direction. The loose packing of the CZ and FWDZ litho-structural facies, and the high alteration prevented reliable sampling for microstructural observations on these fault elements.

At the millimetre-scale, the original primary (sedimentary) texture of the litho-structural facies are overprinted by systematic microfabric, made up by conjugate systems of disaggregation-deformation bands arranged at high- and low-angles with the fault trace, and resembling Riedel-type, P-R-R' shear systems (Figure 9a–d).

The samples coming from HWMZ and FWMZ show a high degree of ductile deformation with asymmetric hydroplastic microfolding, with the same shear sense and direction as the mesoscale folds observed in the HWDZ and HWDZ, along with pervasive lithologic mixing at the grain size scale and pervasive development of low-angled disaggregation-deformation bands.

Another systematic feature observed in these samples is the bimodal pore size distributions (see below), with positively skewed 1st and negatively skewed second mode values, highlighting the bulk contributions of two main classes of pores/openings separated by a threshold at approximately 5 μm (Figure 9e; complete database in DR 2).

The cementation trends observed in backscatter electron SEM-EDS images confirm the mesoscale observations on a systematic Fe-sulphide (i.e. pyrite) cement, which become progressively more important towards subsidiary synthetic HW faults (sometimes marking the transition from the HWDZ to the HWMZ), and in general towards the CZ. Pyrite mineralization varies from sparse nodules in the HWDZ and HWMZ, to a completely pyrite-cemented, fault trace-parallel halo in a mm- to dm-wide area immediately adjacent to the discontinuous slip surfaces (Figure 9f). Apart from localized grain cracking and flacking (i.e. mechanical abrasion of grain boundaries) within stress bridges inside the microlithons, no pervasive cataclasis is observed (Figure 9g–h). Instead, local particle rotations, lithologic/grain size mixing, plastic deformation of clay minerals and cement/matrix-supported zones, suggest creation of interparticle space and plastic deformation of the ductile features during the deformation (Figure 9i–k). The sedimentary injections-type structures that sometimes comprise the HWMZ are characterized by a massive, structureless appearance, consistent with complete obliteration of the original texture, and usually bear subangular and subrounded microclasts of the finer-grained HW and FW wallrock (see Figure 5b). These early fabric features are locally, incrementally reworked/reactivated as microcracks, and subordinately as microshears towards the CZ, suggesting a progressively more brittle regime with time. This brittle overprint is particularly evident in the Negerpynten planar faults (Figure 9l).

The observed microfabric variations across the fault architectures coincide with changes in porosity, pore size and density, consistent with a litho-structural control on diagenesis (Figure 10). The porosity pattern shows a decreasing trend from the HWDZ to the FWDZ, in line with the obvious lithological transition from the sandstone-dominated HW to the shale-dominated FW, with punctuated increase in the inner HWMZ due to localized dilation of granular material (Figure 10a). The marked density increase in the innermost fault envelope reflects the localized Fe-sulphide mineralization (Figure 10b). Due to the systematic bimodality of the results (see above), the median pore size show highly variable values across the fault zone, with large data scatter (Figure 10c). Interestingly, this dispersion narrows when the two single, minor and major modes are considered separately (Figure 10d,e), defining two main trends. The first mode values mimic the cumulative trend, suggesting a diffused primary (matrix) control on pore size distribution, with Gaussian-type end-members and pore size <5–10 μm, and one order of magnitude difference from pristine HW sandstone FW silt-mudstones (see Figure 10d). The second mode values on the other hand show an increase towards the fault core, regardless of the lithologies, with spiky/heterogeneous end-


(a)
N
B
S

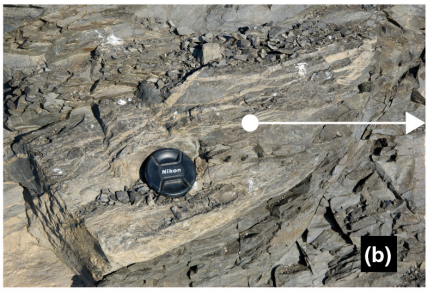
(b)

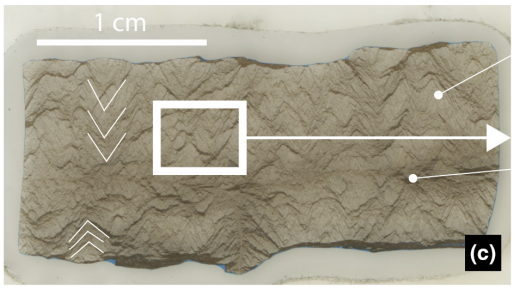
1 cm
(c)

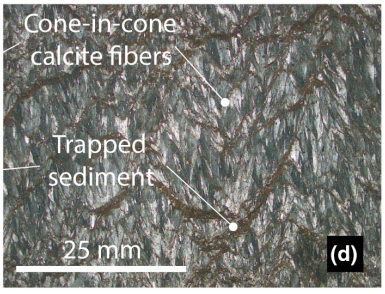
Cone-in-cone calcite fibers
Trapped sediment
25 mm
(d)

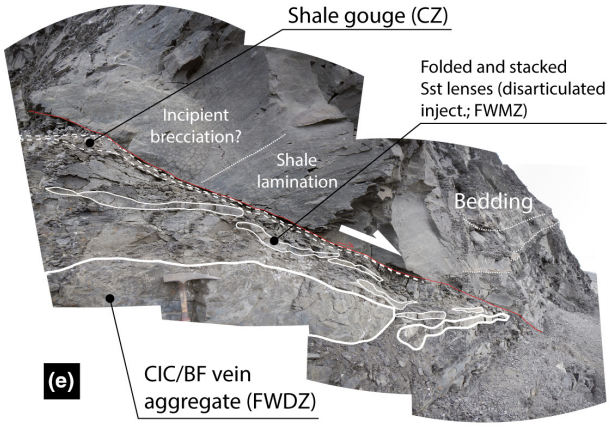
Shale gouge (CZ)
Folded and stacked Sst lenses (disarticulated inject.; FWMZ)
Incipient brecciation?
Shale lamination
Bedding
(e)
CIC/BF vein aggregate (FWDZ)

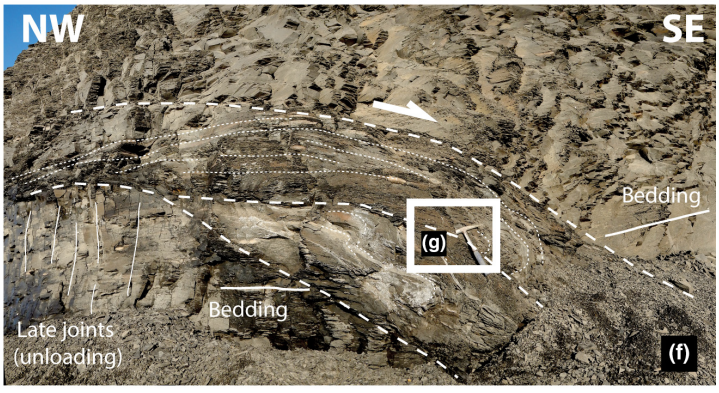
NW
SE
Bedding
(g)
Bedding
Late joints (unloading)
(f)


Folded CIC (FWMZ)
(g)


N
S
1 m
(h)

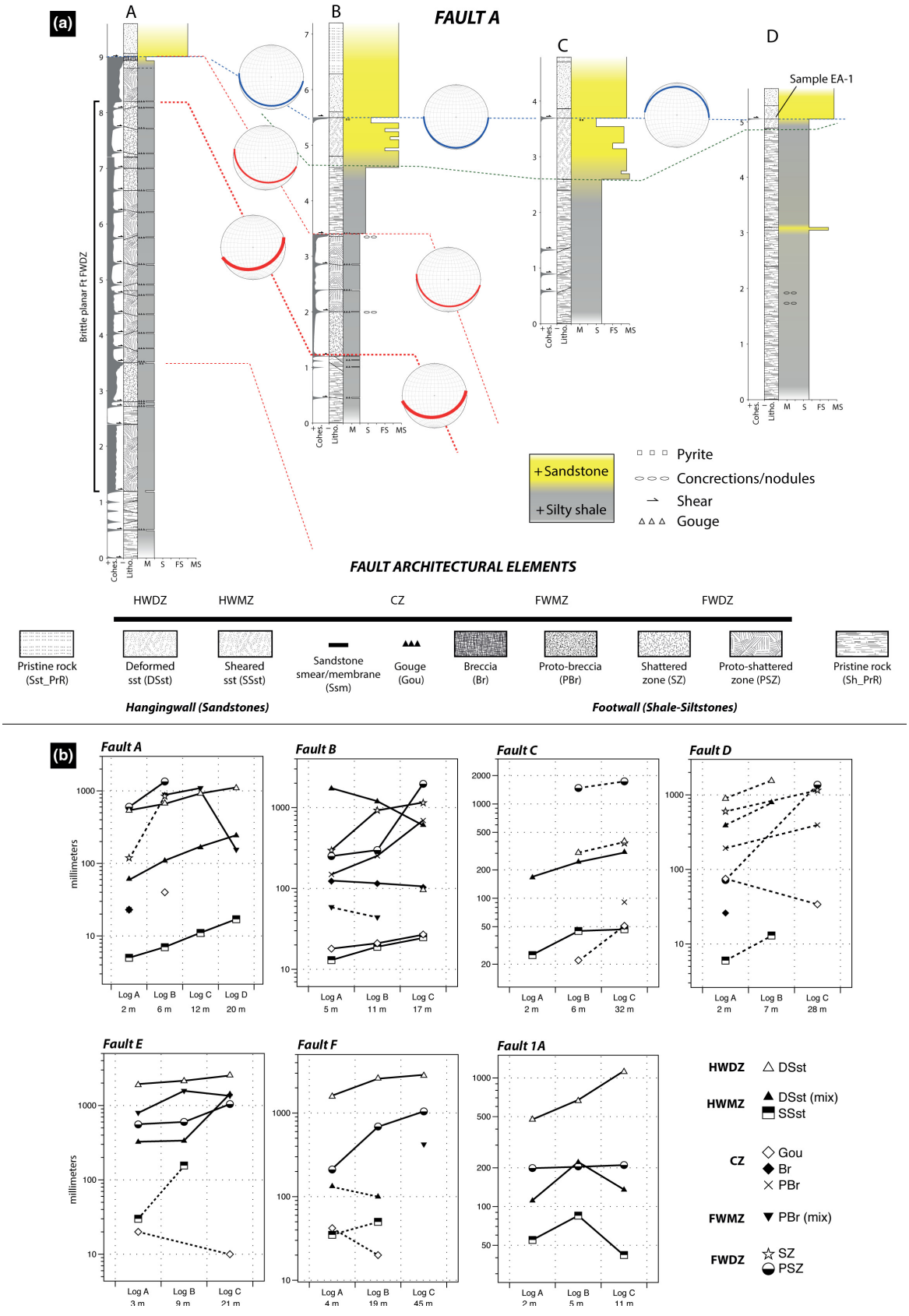

FIGURE 7 Litho-structural fault logs: (a) Example of a correlated fault logs constructed for Fault a (the complete correlation panel for all investigated faults is provided is in DR 1). (b) Logarithmic FFs thickness versus relative displacement (fault logs positions) diagrams for the investigated faults. Note the general increasing trends along with relative increasing displacement, apart from FWMZ and HWDZ, and some CZ elements

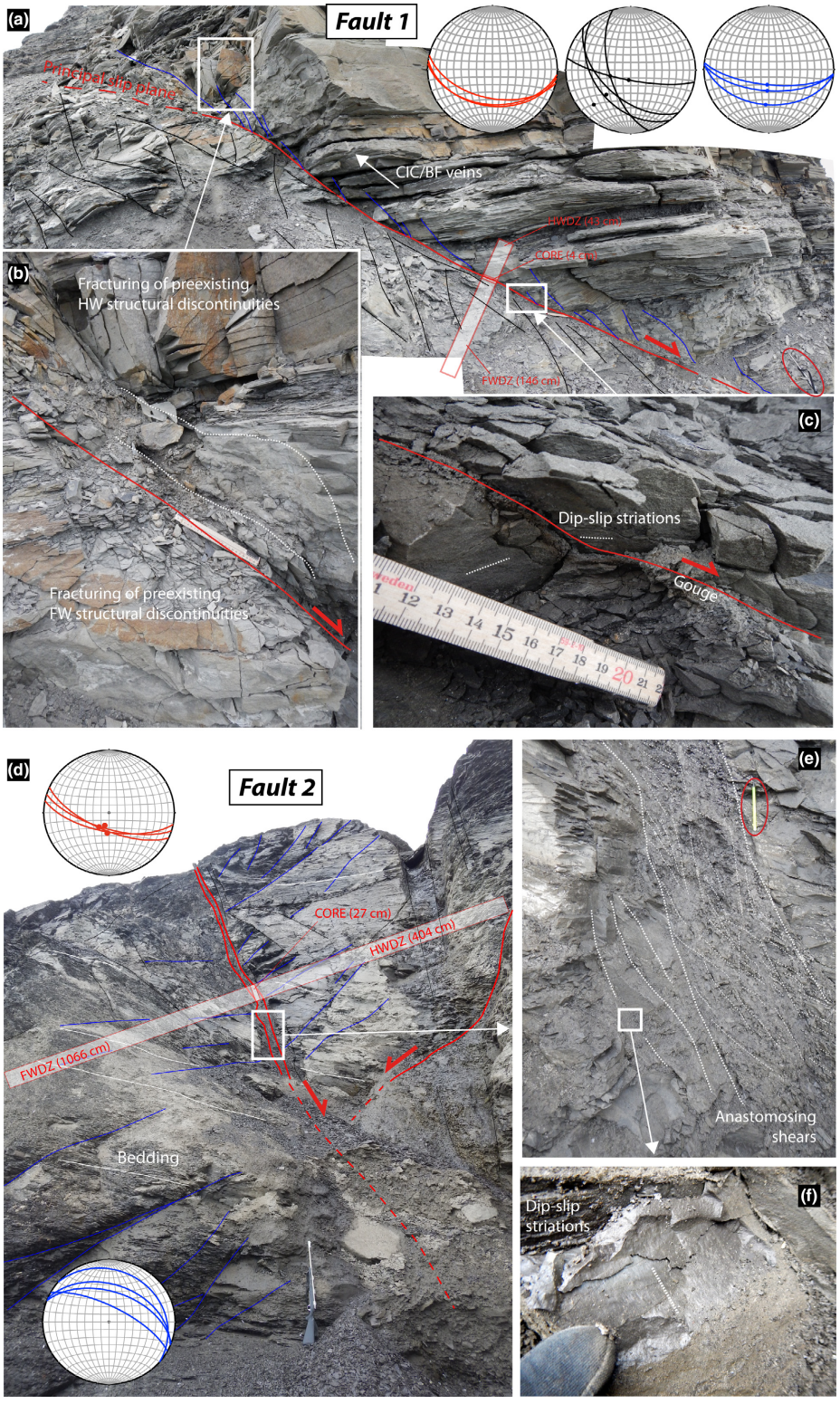

FIGURE 8 Planar (first order) faults investigated at Negerpynten. (a) Overview of Fault 1 with line-drawing and stereoplots of principal slip planes (red) and hangingwall (blue) and footwall (black) shears (dots are striations directions). Rifle for scale (ca. 150 cm). (b) Sheared, liquidized sandstone lens aligned to the hanging wall shears, which likely represent a remnant of HWMZ preserved in the hanging wall from the previous hydroplastic fault phases. Folded metre stick for scale (ca. 22 cm). (c) Detail of the narrow (1 cm) fault gouge interval of the CZ bounded by striated surfaces. (d) Overview of Fault 2 with line-drawing and stereoplots of principal slip planes (red) and shears (blue) and labelling of the bedding (dots are striation directions). Rifle for scale (ca. 150 cm). (e) Detail of d showing the CZ and the inner parts of HWDZ and FWDZ. Note the sigmoidal appearance of the innermost FWDZ created by anastomosing shear surfaces and defining an attached footwall lens. Pencil for scale (ca. 10 cm). (f) Detail of the striations on the bounding surfaces of the attached footwall lens depicted in E. Gloved finger tip for scale

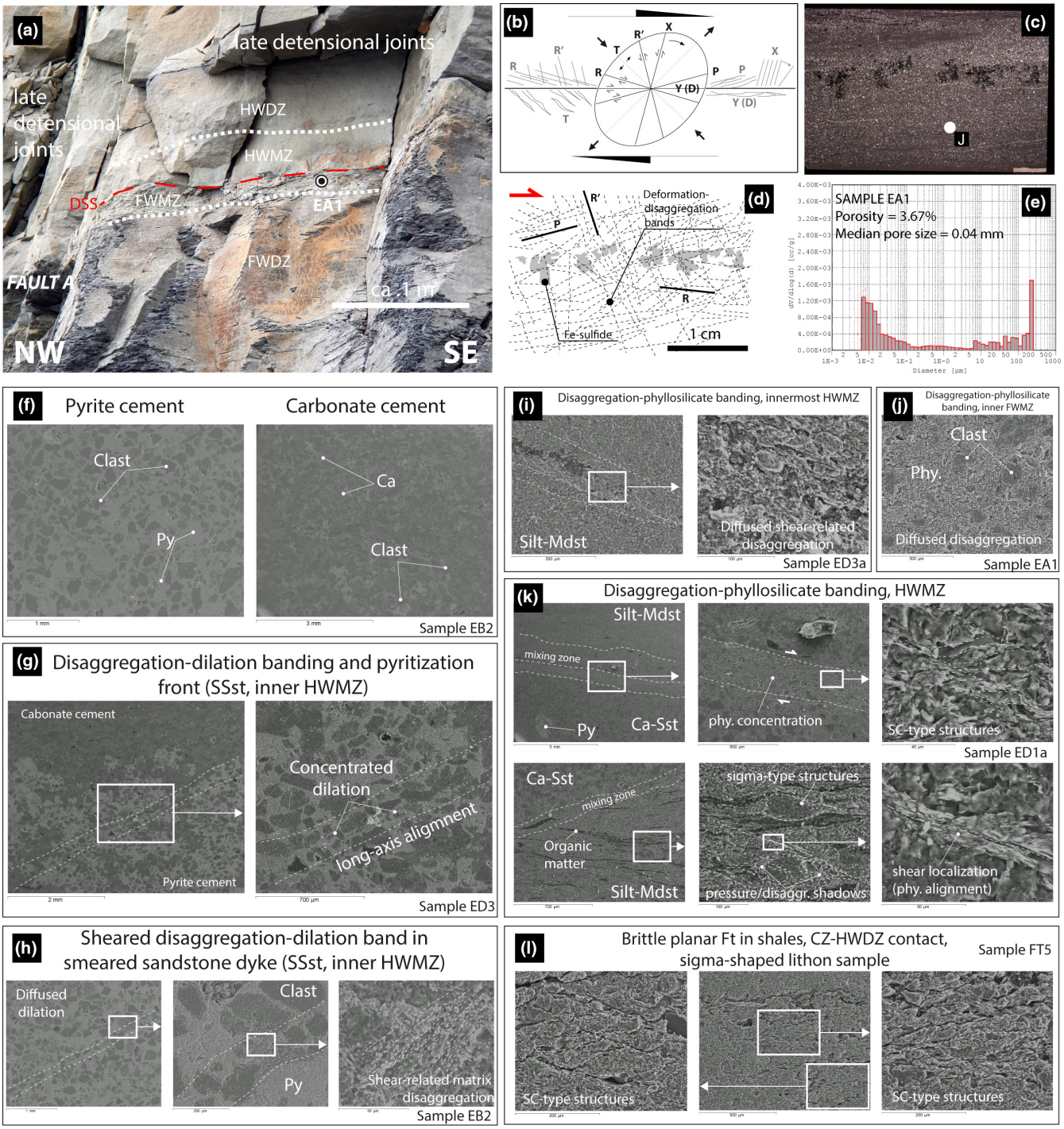

FIGURE 9 Examples of the results obtained from the microstructural and petrophysical analyses (a–e), and BSE SEM/EDS images (f-l). (a) Overview of the gently dipping part of Fault a with labelling of the main AEs and location of the sample EA1 (the complete database is provided is in DR 2). (b) conceptual representation of simple shear-related, Riedel-type structures. (c–e) Thin section and related microstructural interpretation, and pore size diagram of the sample EA1. Note the multimodal trend (see cumulative plots in DR 2). (f) Fe-sulphide (pyrite) versus carbonate (calcite/dolomite) cement in the HWDZ and HWMZ. (g) Deformation-disaggregation (dilation) bands and iron-oxide mineralization front in SSst of the HWMZ. (h) Grain alignment and SC-type microstructures in deformation-disaggregation band in sheared sandstone intrusion involved in the HWMZ. (i) Deformation-disaggregation band cored with sheared phyllosilicates in the innermost HWMZ. (j) Deformation-disaggregation phyllosilicates band in the inner FWMZ. (k) Close-up examples of deformation-disaggregation phyllosilicates bands in the HWMZ. (l) SC-type, anastomosing structures and microduplex in the sheared shales of the CZ-HWDZ contact zone of brittle planar faults

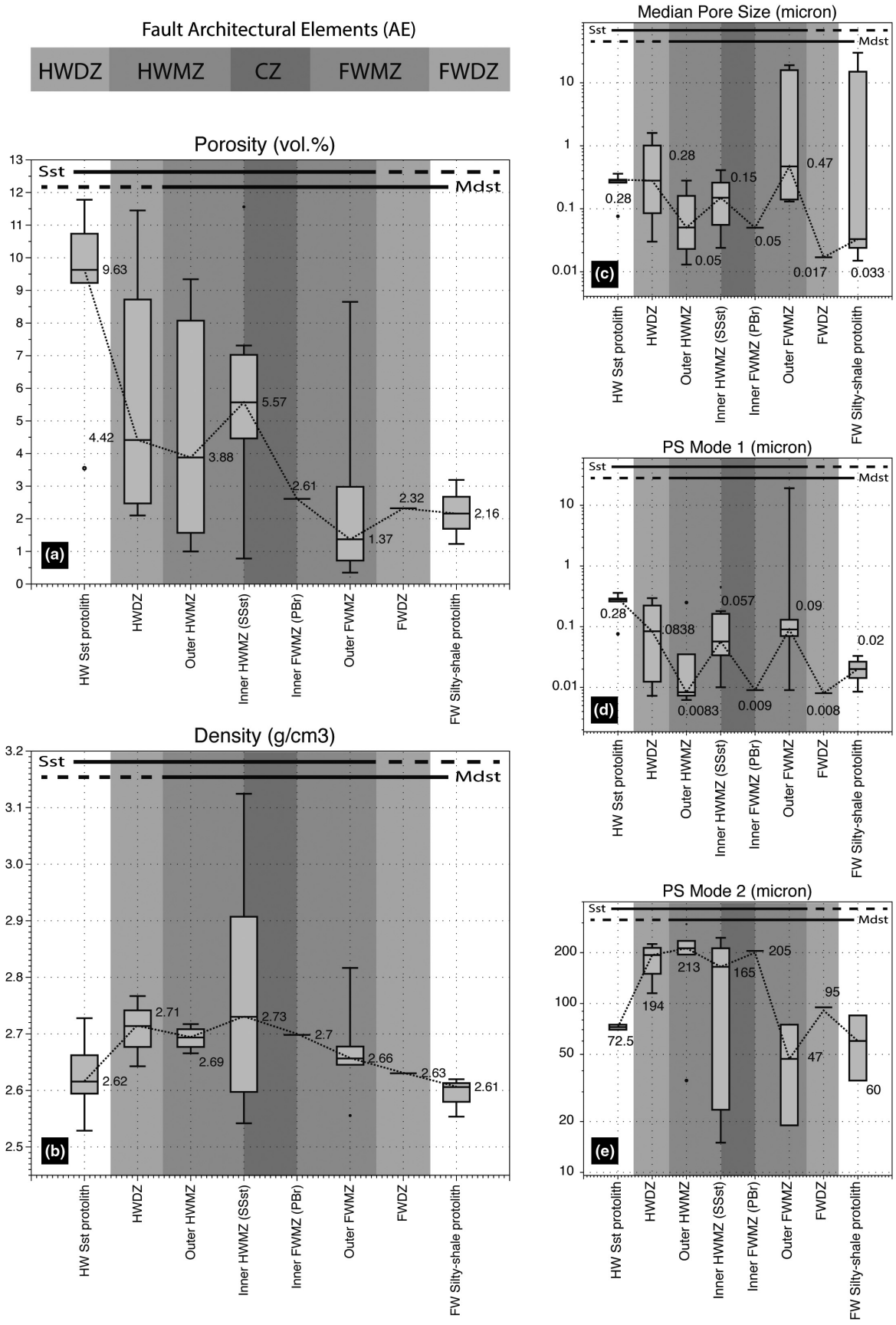

FIGURE 10 Summary of petrophysical parameters across the fault envelope. (a) Porosity. (b) Density. (c) Median pore-size. (d) First modal pore-size. e. Second modal pore-size. Relative sandstone-mudstone content indicated for end-member comparison

FIGURE 11 Examples of plastic, shear-flow structures and soft sediment deformation intervals in the third-order detachments (a–g) and local, mesoscale extensional and compressional features at top Botnheia Fm., where second-order faults sole out (H-N). (a) Slump-type folds. Hammer for scale. (b) Detached sand pillows. Gloved fingertip for scale. (c) Sand load casts and pillows in liquidized interval. (d) Detail of the sandy load casts and attached pillows. Camera lens cap for scale (ca. 7 cm in diameter). (e) Soling out interval in the lower part of Fault b. Note the fault-parallel sand injection in the left-hand side that became progressively shalier downward (towards the right). (f) Detail of E showing the "mud-sand breccia" appearance of the lower tip of the of the up-going sand injection shown in Fig. Camera lens cap for scale (ca. 7 cm in diameter). (g) Detail of the soling out interval showing a completely mixed, liquidized mud-sand interval. Camera lens cap for scale (ca. 7 cm in diameter). (h) Detail of the soft sediment sandy elements embedded in silty-muddy matrix. (i) Detail of asymmetrical hydroplastic fold from the same interval. Circled backpack for scale (ca. 70 cm). (h) Fault tip mono line developed in the cemented Botnheia Fm., which enucleates a listric growth fault in the overlying Tschemakfjellet Fm. (i) Soling out lower part of Fault d. Note the hanging wall syncline-anticline, enhanced by bed dragging. (j) Thrust zone in the cemented Botnheia Fm.. showing a drag fold with a top-to-the-right shear sense. Person for scale. (k) Thrust stack developed in the cemented Botnheia Fm. between Fault b and Fault c. Circled Zodiac for scale (ca. 2 m). (l) Duplex structure in the thrust zone shown in d developed at expenses of a fine sandstone bed. Circled pencil for scale (ca. 10 cm). (m) Folded interval of the second-order detachments involving silty-shale lithologies and CIC/BF layered aggregates. Person for scale (ca. 7 cm in diameter). (n) Folded CIC/BF layered aggregate with layered veins of blocky calcite cutting the hinge zone. Camera lens cap for scale (ca. 7 cm in diameter)

members testifying openings >5–10 μm, consistent with a secondary, superimposed (structural) control (see Figure 10e). Complex relationships arise in the HWMZ and FWMZ due to lithological mixing (e.g. in Figure 9e).

4.4 | Detachment interval(s)

The third- and second-order fault detachment intervals are, respectively, contained within the lower, fine-grained Tschermakfjellet Formation (Figure 11a-g) and the transitional zone atop the Botneheia Formation (Figure 11h-n). Both display hydroplastic shear-flow structures and ductile/plastic soft sediment deformation intervals, within distal delta front depositional environments in the first case, and organic-rich offshore basinal shales in the second. The most common structures are slump-type, noncylindrical folds and loading structures (e.g. load casts and ball-and-pillows), observed to progressively evolve from attached to detached with proximity to the core of the shear zones (Figure 11a-d). In these shear zones, cm- to metres-thick, hydroplastically deformed sandstone-dominated elements appear folded, sheared and rotated, with the development of pseudopressure shadows, tails and inclusion trails, revealing a shear sense compatible with the displacement of nearby fault tips and traces (Figure 11e–g).

Local, mesoscale compressional and extensional features are observed in the lowermost organic shale interval, directly overlying a well-cemented, phosphate-rich interval that marks the transition with the Botneheia Formation (second-order faults detachment interval). In the inner part of Tjuvfjorden bay, about 2 km NE to the Øhmanfjellet study site, the top of the Botneheia Formation is folded into monoclinal geometries draped by silty shales, that seem to localize the nucleation points of the overlying growth faults (Figure 11h,i).

Outcrop-scale thrust splays, discrete thrust and low-angle normal faults with associated drag folds and duplex structures are also locally observed (Figure 11j–l). Other low-angle, cm- to metres-thick shear zones with normal and reverse movements contain isoclinally folded CIC lenses (Figure 11m,n), similar to those observed in the FW and CZ of the dipping part of the second-order growth faults and their associated detachment (see e.g. Figure 6).

5 | DISCUSSION

5.1 | Growth fault architectures and deformation mechanisms

The lateral-vertical geometric relationships of the architectural elements (AE; fault core zones CZ, mixed zones MZ and damage zones DZ), suggest a general widening of the soft-sediment deformation products along with increasing displacement, which transition downward into detachment zones represented by relatively thick intervals of remoulded and mixed lithologies (see Figures 7b and 11a–g). Such original relationships are maintained in the third-order growth faults, which are preserved and passively deformed and rotated within the first- and second-order growth fault blocks. On the other hand, the 2nd and especially the first-order faults are characterized by a significant brittle overprinting with strain localization towards in the inner fault zones. Based on the trend and location of the few faults cutting through the De Geerdalen Formation (i.e. post-Triassic; see Figure 2g), we suggest that some of the favourably oriented segments of the first-order faults (and associated second-order ones) eventually interlinked into seismic-scale fault zones crosscutting the entire stratigraphy. Relatively low displacements on these reactivated faults can be explained by the "attenuation" operated by the growth fault interval of the Tschermackfjellet Formation (see Figure 2g). In this framework, this interval acts as structurally anisotropic buffer zone of mechanical decoupling between well-bedded, under- and over-lying

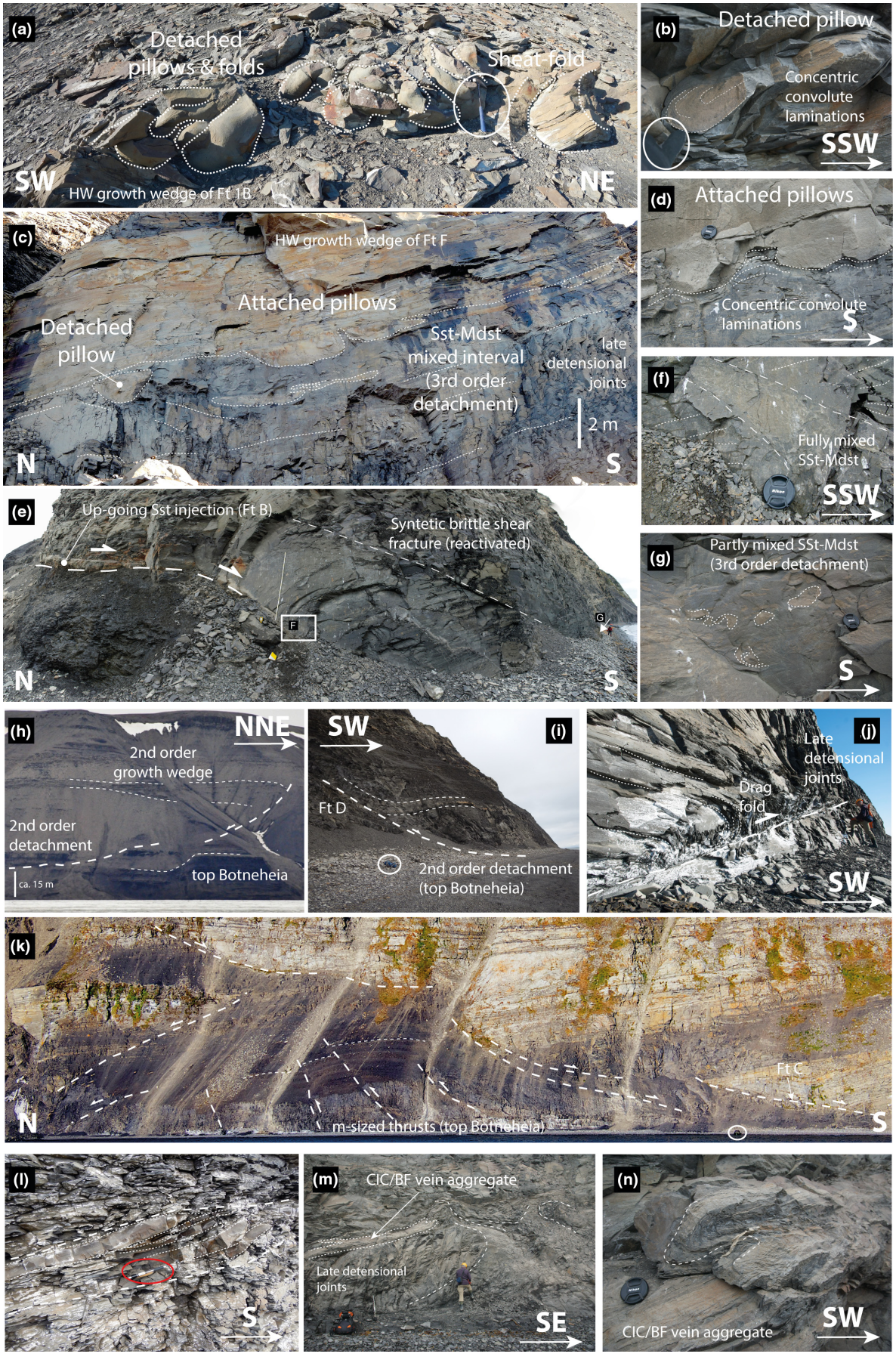
(a)
Detached pillows & folds
Sheat fold
SW
HW growth wedge of Ft 1B
NE
(b)
Detached pillow
Concentric convolute laminations
SSW
(c)
HW growth wedge of Ft F
Attached pillows
Detached pillow
Sst-Mdst mixed interval (3rd order detachment)
late detensional joints
2 m
N
S
(d)
Attached pillows
Concentric convolute laminations
S
(e)
Up-going Sst injection (Ft B)
Syntetic brittle shear fracture (reactivated)
F
G
N
S
(f)
Fully mixed SSt-Mdst
SSW
(g)
Partly mixed SSt-Mdst (3rd order detachment)
S
(h)
NNE
2nd order growth wedge
2nd order detachment
top Botneheia
ca. 15 m
(i)
SW
Ft D
2nd order detachment (top Botneheia)
(j)
Late detensional joints
Drag fold
SW
(k)
Ft C
N
m-sized thrusts (top Botneheia)
S
(l)
S
(m)
CIC/BF vein aggregate
Late detensional joints
SE
(n)
CIC/BF vein aggregate
SW

FIGURE 12 (a) Evolutionary cartoon illustrating the stepwise, conceptual progressive deformation from ductile to brittle deformation regime along with burial/lithification inferred for the investigated faults, with emphasis on the sandstone-shale and shale-shale juxtaposition parts. (b) Summary figure depicting fault hierarchy (based on the type of detachment) and mutual relationships, with indication of the possible formation setting. (c) Synoptic logs showing the petrophysical variations observed across the fault envelope. (d) Conceptual profile showing the local growth sections' distribution and local differential compaction sedimentary loading inferred to enucleates the different types of faults. (e) Reconstruction of the possible palaeogeographic setting, sedimentary and structural processes, with indication of the regional differential sedimentary loading-compaction

sequences, with subhorizontal accommodation of the deformation (e.g. rotation of second-order fault blocks).

This progressive reworking of soft-sediment structural discontinuities indicates shallow multistage growth faulting, achieved through micro to mesoscale polyphased deformation controlled by rheological-mechanical changes during progressive burial, shallow diagenesis and lithification. This suggests a syn-tectonic, plastic/ductile (*sensu* Rutter, 1986) to brittle regime transition, from distributed strain (hydroplastic phase) to strain localization (brittle phase) end-members (Figure 12a).

In particular, this polyphase evolution is recorded by the superposition and mutual overprinting of different deformation mechanisms. In the sandier HW, these vary from 1) an early stage of independent particulate flow aided by localized liquidization (i.e. liquefaction + fluidization; Allen, 1982) phenomena of granular material due to excess pore pressure, testifying to the unconsolidated and water-saturated state of the lithologies, 2) an intermediate stage of localized particulate flow aided by limited grain breakage and 3) a later stage of fracturing along structural and diagenetic discontinuities such as deformation band swarms and oxidation/reduction fronts. In the silt/shale-dominated FW, the deformation evolves from 1) an early stage of (hydro)plastic deformation, 2) an intermediate stage where the state of stress is between the elastic limit of the material and its breaking strength, and thus exhibiting both elastic and plastic properties (e.g. elasto-plastic deformation; lithological mixing), to 3) a later stage of diffused fracturing in low porosity rocks (e.g. shattered and brecciated shales; see Figure 12a). On the basis of the main driving mechanism and the inferred state of material during deformation (see e.g. Balsamo et al., 2013), the extrapolated detachment depth ranges from a few metres to ca. 30–40 m for the third-order faults, and down to 100–200 m for the second-order ones. The different conceptual phases depicted in Figure 12a represent the "frozen-in" status for any given fault and position along the fault itself. In this picture, these single evolutionary steps and/or locations along the fault envelope are recorded by different fault facies associations (FFAs), being also characterized by different preservation potential depending on the fault hierarchy (see Figure 12a).

In some cases, entrainment of FWMZ and HWMZ lenses of second-order faults into the CZ of first-order support the subsequent reactivation of some of the favourably oriented segments of listric faults into planar faults, eventually linking to the later faults crosscutting the De Geerdalen Formation (see above).

5.2 | Petrophysical evolution and structural diagenesis

The variation in deformation intensity across the growth fault zones and along their displacement direction is mirrored by microstructural-petrophysical changes. Microfabric-related structural anisotropy controls porosity-permeability and promoted localized microfracturing as suggested by the systematic bimodal pore size distributions. Greater data variability in porosity recorded in the HWMZ and FWMZ are due to enhanced pyrite mineralization and high degree of lithological mixing. In particular, evidence of a microscale "dual poro-perm" system is derived from the systematic bimodality in the pore size diagrams (see Figure 9e and DR 2). This pattern has been interpreted as the result of microcracking along the structural discontinuities (e.g. deformation-disaggregation/compaction bands) making up the microfabric network (i.e. petrophysical framework-related permeability anisotropy; Cavailhes et al., 2013). On the basis of the SEM data and as suggested by Bolton, Maltman, and Fisher (2000), this bimodal grain size distribution is inferred to be in line with the estimated grain size (positively skewed first mode recording primary depositional grain packing affected by normal compaction) and measured microcrack dimensions (negatively skewed second mode recording secondary microfracture network favoured by structural heterogeneity and directional anisotropy). In this framework, the two lithological and structural inputs appear to be separated into primary (sedimentary) and secondary (fracturing) contributions, changing vertically (and laterally) along the fault zone (see Figure 10b–c). In this framework, the bulk contribution to fluid storage and motion during deformation is provided by the progressive superposition of a secondary porosity due to microcracking along structural discontinuities onto a primary matrix porosity, which is in turn modified by increasing dilation, grain packing rearrangement, cementation and limited grain cracking.

Simple shear- and dilation-related textures are observed in association with matrix/cement-supported fabric and

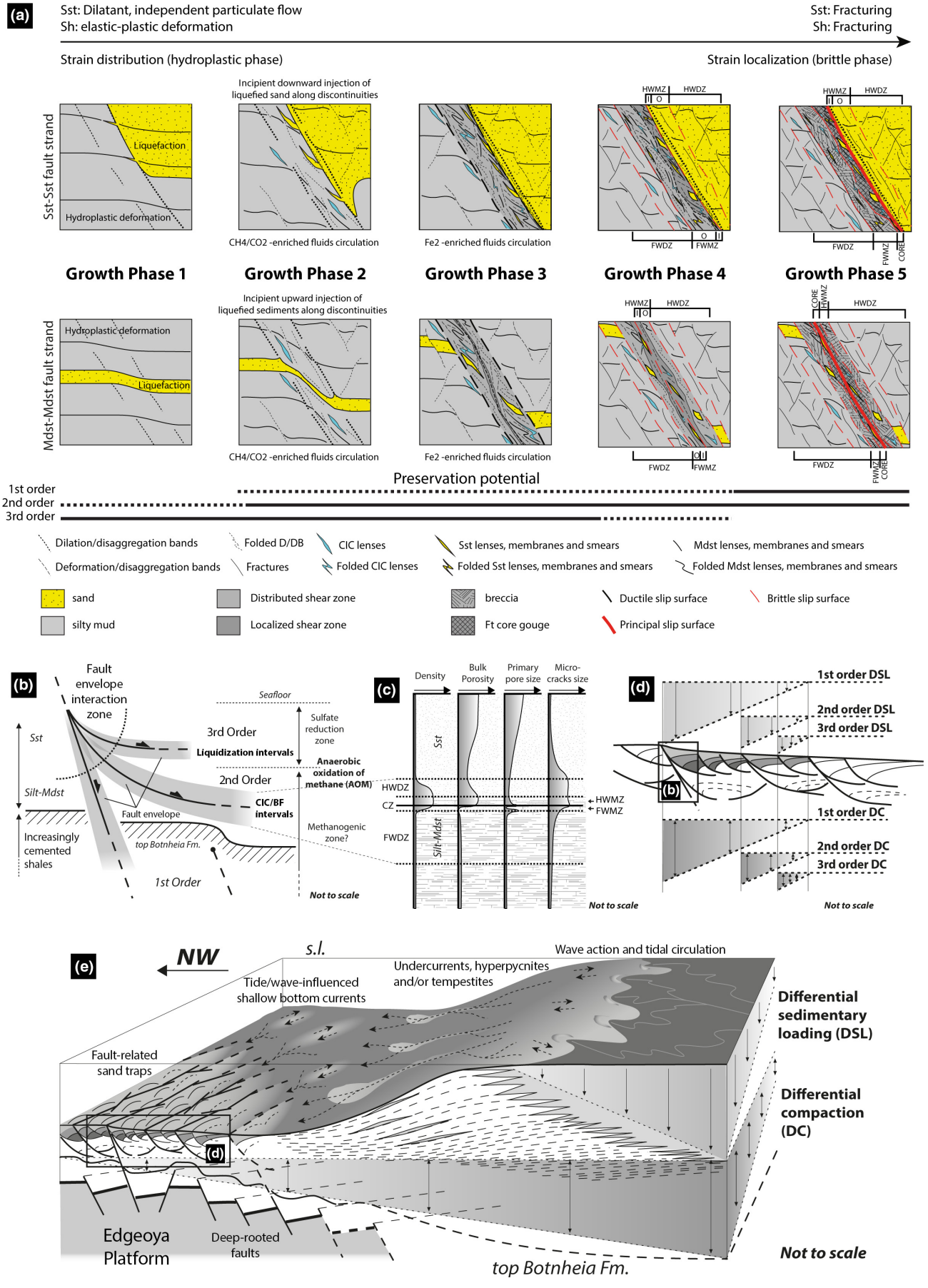
(a)
Sst: Dilatant, independent particulate flow
Sh: elastic-plastic deformation
Sst: Fracturing
Sh: Fracturing
Strain distribution (hydroplastic phase)
Strain localization (brittle phase)
Sst-Sst fault strand
Liquefaction
Hydroplastic deformation
Incipient downward injection of liquefied sand along discontinuities
CH4/CO2 -enriched fluids circulation
Fe2 -enriched fluids circulation
HWMZ
HWDZ
FWDZ
FWMZ
CORE
Growth Phase 1
Growth Phase 2
Growth Phase 3
Growth Phase 4
Growth Phase 5
Mdst-Mdst fault strand
Hydroplastic deformation
Liquefaction
Incipient upward injection of liquefied sediments along discontinuities
CH4/CO2 -enriched fluids circulation
Fe2 -enriched fluids circulation
Preservation potential
1st order
2nd order
3rd order
Dilation/disaggregation bands
Deformation/disaggregation bands
Folded D/DB
Fractures
CIC lenses
Folded CIC lenses
Sst lenses, membranes and smears
Folded Sst lenses, membranes and smears
Mdst lenses, membranes and smears
Folded Mdst lenses, membranes and smears
sand
silty mud
Distributed shear zone
Localized shear zone
breccia
Ft core gouge
Ductile slip surface
Principal slip surface
Brittle slip surface
(b)
Fault envelope interaction zone
Seafloor
Sst
Silt-Mdst
3rd Order
Liquidization intervals
Sulfate reduction zone
Anaerobic oxidation of methane (AOM)
2nd Order
CIC/BF intervals
Fault envelope
Increasingly cemented shales
top Botnheia Fm.
Methanogenic zone?
1st Order
Not to scale
(c)
Density
Bulk Porosity
Primary pore size
Micro-cracks size
Sst
Silt-Mdst
HWDZ
CZ
FWDZ
HWMZ
FWMZ
Not to scale
(d)
1st order DSL
2nd order DSL
3rd order DSL
1st order DC
2nd order DC
3rd order DC
Not to scale
(e)
NW
s.l.
Wave action and tidal circulation
Undercurrents, hyperpycnites and/or tempestites
Tide/wave-influenced shallow bottom currents
Fault-related sand traps
Differential sedimentary loading (DSL)
Differential compaction (DC)
Edgeoya Platform
Deep-rooted faults
top Botnheia Fm.
Not to scale

localized, dispersed grain packing, especially within Fe-sulphide cemented zones. A microstructural control on the calcite and pyrite cement distribution is also apparent, with a systematic occurrence of Fe-sulphide impregnated haloes in the sheared and smeared sandstone elements within or in the close proximity of the CZ and surrounding discrete shear surfaces in the HW (see Figure 9). Such dilation conditions favoured early circulation of formation fluids enriched in Fe_2 in the sandier HW of the shallower faults (3rd order) leading to the localized pyrite cementation. At deeper stratigraphic levels, mineralizing (CH4-enriched?) fluids circulation in the second-order fault zones is suggested by the occurrence of CIC/BF vein aggregates, arranged as elongated fault-parallel lenses, progressively folded towards the CZ. The presence of these localized calcite mineralizations in the FW of some third-order faults and within the detachment of the second-order faults, along with their change in shape and size (from isolated cm-sized veins to m-sized, lenticular composite vein aggregates respectively), testify to early fluid flow communication along the fault zones, and a structural control on their distribution.

This structural-diagenetic framework may suggest the combined contribution of fluid seepage forces (up to overpressure?) and flow, associated with pore pressure gradients due to differential compaction-dewatering in poorly consolidated sediments at shallow burial conditions (<300 m depth), and leading to the shear strength reduction of the second- and third-order faults, as hypothesized by Maher et al. (2017). This possible scenario is in line with a very shallow environment (few metres to tens of metres below the seafloor), between the methanogenic and the sulphate reduction zone (Anaerobic oxidation of methane or Sulphate Methane Transition; e.g. Mitterer, 2010), marking the boundary between a lower zone were anaerobic bacterial oxidation of CH_4 enhances calcite precipitation and CIC/BF development, from an upper zone were sulphate reduction favours pyrite mineralization (Figure 11b), as described by Meng, Hooker, and Cartwright (2017). The hydrocarbon decomposition-aided, microbialitic origin of some sedimentary CIC structures in the same lithologies of eastern Svalbard studied by Tugarova and Fedyaevsky (2014) is in line with the present observations. These diagenetic boundaries are susceptible to variations in the basin-scale, boundary environmental conditions (e.g. pressure-temperature variations at the seafloor), and likely represent preconditioning factors in the development of density-gravity instabilities that eventually can contribute to extensional listric faulting (see Figure 11b, c). Similar diagenetic features have been recognized elsewhere in the Triassic record of eastern Svalbard unrelated to growth faulting but attributed to near-surface biological processes (Tugarova & Fedyaevsky, 2014). Analyses on C-O stable isotopic signatures to shed light on these issues are currently ongoing.

5.3 | Growth wedges stratigraphy and depositional setting

Three main types of growth wedges are recognized: 1) combined, silt/mud- and sand-dominated (pre to late-growth) wedges, related to first-order faulting, 2) sandstone-dominated (late-growth) wedges related to second-order faulting (see below) and 3) intragrowth wedges (syn-growth) related to third-order faulting. The stacking patterns of the sandstone-dominated wedges, and the geometrical (i.e. erosion-deposition) relationships between the major half-graben growth fault sequences reveal that the general infilling trends, and consequent syn-sedimentary faulting, proceeded from N to S, in an overall "progressive," in-sequence fashion (see relationships between growth wedges 1-3 and 4-5 marking the transition between major growth sequences 1 and 2 in Figure 2g). The switch from late-growth (sandstone-dominated) wedges 1 to 2 seems to be achieved though the downward movement of the southern block during the deposition of the growth wedges 3 (see Figure 2g). This is in line with the stacking patterns observed for the different the facies associations comprising the late-growth wedge, sandstone-dominated sequences (Osmundsen et al., 2014). Notably, at the scales covered by our observations it is also possible to recognize that the initial phases of listric faulting (up to growth wedge 2) produced approximately symmetric graben-type sags bounded by both S to SSW and N to NNE dipping faults and characterized by dominant fine-grained sedimentary infill (see Figure 2g). The asymmetric half-grabens developed in the later stages (from growth wedge 2 and up), along with increasing sand-rich sedimentary input and enhanced activity on the S to SSW-dipping faults (see Figure 2g). This, combined with the increasing dominance of first-order faults to the SE proceeding from Kvalpynten to Negerpynten (see Figure 2c,d) seems to confirm the control of the latter on the development of the second-order ones to the NW of the study area. Notably, this seems in contrast with the original interpretation of a retrogressive delta-front slope collapse of a S-SW directed delta system, as postulated by Edwards (1976).

The silt/shale-dominated parts of growth wedges (i.e. pre and early growth), along with the continuous draping shale interval atop the growth faulted interval, share the common features of prodelta deposits, with punctuated evidence of sandstone lobes, especially towards the top of the sequences. In this framework, the four time-equivalent stratigraphic surfaces representing the upper boundaries of the late-growth wedges 1 to 3 (see Figure 2e–g) are interpreted as transgressive surfaces with a seafloor-exposure

(e.g. hard-ground) surfaces developed on top of late-growth wedge 4 according to Smyrak-Sikora et al. (2017). The internal stratigraphy of the syn-growth sandstones shows combined characteristics of wave-tidal deposits (e.g. subaqueous tidal bars and dunes). The same succession is observed at the base of the De Geerdalen Formation which overlies the draping shale interval and is interpreted to record a progressive transition from tide/wave-dominated delta front to delta top environments (see Haile et al., 2018; Osmundsen et al., 2014).

According to this scenario, "delta front lobe(s)" deposited by the remobilization of classic delta front and mouth bar sands by floods (e.g. hyperpycnal flows) and/or storms (e.g. surge return flows) would be reworked by tidally and/or downwelling-influenced, along-shore, shallow bottom-currents to be reoriented as sand bars parallel to the strike of active (1st order) faults and infilling their related superficial bathymetric depressions (see e.g. Pochat & van den Driesse, 2007). The degree of reorientation would depend on the amount of fault-generated physiography of the seafloor and amount of generated relief, which can be quantified by the maximum thickness of the sedimentary growth wedge infills (e.g. metres for the third-order wedges and tens of metres for second-order ones).

Beside the structural-stratigraphic relationships preserved in the HW sandstone wedges, evidence of palaeo-bathymetric complexity is also suggested by the unconformities observed in the FW silt-mudstone succession, interpreted as mixed nondeposition and/or erosion surfaces. Moreover, their localized cementation, strikingly similar to the one characterizing the top of Botnheia Formation, testifies *in situ,* early (phosphate-related) diagenesis and prolonged seafloor exposition (see Krajewski, 2011, 2013).

Additionally, while significantly disperse, the mean strike direction of the growth faults along the virtual NNW-SSE transect crossing the investigated sites in southern Edgeøya seems aligned with the local palaeo-current orientations, supporting the early fault-related control on sediment distribution (see Figure 2). Fault strikes seem to follow the wave ripple crest trends, which, in turn, are inferred to express an articulated and locally strongly curving palaeo-coastline. Haile et al. (2018) also argues for such a palaeo-coastline geometry.

This type of depositional setting would have favoured differential compaction-driven subsidence between the prodelta and the relatively more proximal zones, leading to the creation of landward-dipping listric growth faulting at the delta toe (Back & Morley, 2016; Braathen et al., 2017). In this framework first order and larger-scale (seismic) faults with spacing in the order of kilometres would provide a counter-regional, monoclinal slope dipping towards the delta system. This gentle (ca. 1-3 degrees) slope would be affected by a relatively uneven physiography, with local seafloor relief created by synthetic (and antithetic) second- and third-order fault systems. The resultant half-graben depozones would have been able to trap deltaic sands redistributed by mass wasting and along-coast (wave- and tidally influenced) offshore currents, enhanced by the localized structural confinement of the depositional setting. The increase in localized sedimentary loading and the consequent retreat of the compaction front would have progressively activated growth fault sequences in a landward direction, as documented in this work. Localized differential compaction and sedimentary loading, and consequent disequilibria are inferred to influence growth faults activity also at lower scales, within the second- and third-order sandstone wedges (Figure 12d). In this framework, the monoclines atop the Botneheia Formation are likely related to the development of a trishear zone of deformation above deep-rooted fault tips, roughly striking in the same direction as the first-and second-order growth faults, and testify to the creation of syn-sedimentary relief and consequently uneven seafloor topography during the deposition of the lower Tschermakfjellet Formation. In other words, these can be considered as earlier first-order faults that simply did not reactivate later on.

5.4 | Growth fault distributions and possible causal mechanisms

According to the literature and supported by presented data, the investigated growth fault systems develops in the prodelta region of a large Triassic delta systems. This progrades across relatively shallow, epeiric (epicontinetal) shelfal basins developed in the extended foreland, located between the older Caledonides to the W-SW and the palaeo-Uralides in formation (see e.g. Anell et al., 2016; Klausen et al., 2016). The predeltaic succession is characterized by the deposition in limited water circulation and high-organic supply, as testified by the widespread anoxic conditions periodically recorded on the seafloor (see e.g. Krajewski, 2013). In such a geodynamic situation, combined far-field stress trajectories curve and intersect at different angles and different distances from orogenic front, leading to complex regional deformation and associated network of structural patterns with dominance of high- to low-angle (re)activation of longitudinal, cross and conjugate systems (e.g. Hancock & Bevan, 1987). In this case, the result is a fault-basin oblique inversion of inherited structural architectures (i.e. Carboniferous basins) achieved during the increasing tectonic activity in the E due to the Uralide orogeny in Late Triassic (Klausen et al., 2016). Renewed compression and formation of the West Spitsbergen Fold-and-Thrust Belt (Steel et al., 1985; Braathen, Bergh, & Maher, 1997) during the Cenozoic reactivates the tectonic lineaments arranged into a N-S structural domain

(e.g. Billefjorden in Svalbard, Loppa High in NW Barents shelf) and a NE-SW structural domain (E Svalbard, SW Barents shelf), as shown for instance in Faleide et al. (2008). The interpretation proposed by Anell, Braathen, Olaussen, and Osmundsen (2013), Anell et al. (2016) and Klausen, Ryseth, Helland-Hansen, Gawthorpe, and Laursen (2014), Klausen et al. (2015), is that of a major delta system sourced from the palaeo-Uralides, prograding with a general complex pattern towards the N-NW. This delta system advances above the SE flank of a fault-bounded, elongated and roughly E-W to NE-SW oriented, palaeo-bathymetric high (i.e. Edgeøya platform), with a significant decreasing in the overall accommodation for sediments. This reduction results in lack of aggradation and causes differential advancement rates of the clinoforms, with local delta lobe indentation. Such differential progradation produced local to regional differential compaction at different stratigraphic levels, with the development of frontal (and subordinately lateral) gradients in subsidence. In this scenario, gravitational discharge of a regional, few-degrees slope dipping towards the land is responsible for the creation of an articulated physiography featured by local half-graben depocentres, developed at different scales (Figure 12e).

Due to the systematic areal persistency and parallelism with the regional tectonic lineaments recognized in the area (e.g. Franz-Victoria Basin, Edgeøya Platform), the first-order growth faults likely relate to the surficial expression of major, long-lived and deep-rooted fault systems, inherited from the Palaeozoic (e.g. Marello et al., 2013) and/or lately reactivated. In this framework, the relationships between 1st and second-order growth faults, and the later seismic-scale fault zones (i.e. cutting across the upper draping shale interval and/or across the top Botneheia; see above), can be generally described in term of "soft linkage" (i.e., mechanical decoupling of detachment intervals), with eventual, local evolution towards "hard linkage" (Gabrielsen, Sokoutis, Willingshofer, & Faleide, 2016), where through-going, first-order (and larger) planar fault zones are observed to cluster and cut across the top of the Botneheia Formation (see Figure 12b,e). Due to the listric arrangement of the second-order growth fault array, the (re)exploitation of their favourably oriented branches by later faulting does not result in appreciable vertical offsets, but rather, part of the related deformation is accommodated by cumulative slip displacement in the gently inclined and horizontal segments (see Figure 2g). Accordingly, the growth-faulted interval of the Tschermakfjellet Formation would have act as a "buffer zone" for the vertical, downward propagation of the posttectonic faults.

The development of second- and third-order faults in these first-order growth fault blocks seems related to mechanical-rheological instabilities at distinct stratigraphic intervals, within mechanically weak, bedding-parallel stratigraphic zones prone to be reactivated as detachments, located within the top Botneheia Formation and the prodelta deposits of the lower Tschermakfjellet Formation respectively (diagenetic front and a liquidization level; see above and Figure 12b). In the depicted local to regional palaeo-geographic context, the trigger for the syn-sedimentary movement could be due to tectonic activity on the first-order (and larger) faults, acting as preferential avenues that allow fluid movement and associated diagenesis. This is in turn possibly favoured by localized sedimentation and differential compaction, and changes in the hydrogeological regime (climatically or tectonically controlled, or a combination thereof). In particular, tips of the second-order faults are often associated to local accumulations of sand-rich gravity flow lobes with HCS, suggesting a causal relationship with autocyclic sedimentary processes (e.g. hyperpycnites and/or tempestites; see Figure 12e).

In summary, the processes inferred to control this auto- to allo-cyclic interplay of differential sedimentary loading, faults' activity and creation of sedimentary accommodation, include: (1) shallow substrate remobilization (e.g. from seismic shocks and/or abrupt shifts of diagenetic fronts), (2) increasing grain size and sedimentation rates of clastic input (e.g. distributary channel avulsion, severe climatic events, enhanced continental weathering), (3) redistribution of grain size populations (e.g. segregation of sand- and mud-rich depozones by focused, tidally/storm-induced, along-shore, shallow bottom currents). On the basis of the available data we cannot pick up one major causal mechanism out of the spectrum of the possible proposed ones and dedicated studies are envisioned for a better constrain.

6 | CONCLUSIONS

The Triassic growth fault systems of southern Edgeøya (East Svalbard, Arctic Norway) comprise three orders of faults, with the second- and third-order representing listric faults that control the internal growth parasequences, and intra-(syn) growth wedges respectively. Planar, first-order faults influence the accommodation in both growth stages. The first-order faults and their interlinkage possibly represent the uppermost expression of larger, seismic-scale faults that have been imaged offshore.

The progressive micro to mesoscale brittle reworking of structural discontinuities related to soft-sediment deformation suggests polyphase deformation during progressive lithification and compaction, and records a transition from hydroplastic, distributed strain, to brittle strain localization. This progresses along with the combined evolution of the different orders of faulting and related sedimentary growth wedge cycles, and, ideally, records a gradual shift of the

locus of deformation from the third-order to the first-order fault zone end-members. In HW sandstones, deformation mechanisms vary from liquidization processes and independent particulate flow at low confining pressure causes shear-dilation, to diffused disaggregation and compaction banding with localized incipient cataclasis, eventually leads to localized shear and extensional fracturing. In the FW silty-shales, deformation mechanisms vary from hydroplastic deformation and disaggregation-phyllosilicate tabular shear zones, to diffuse brittle-ductile shearing and later localized shear failure and extensional fracturing. This evolving rheological-mechanical behaviour is due to changes in material properties during burial and shallow diagenesis.

The petrophysical properties of the litho-structural facies comprising the growth fault architectural elements show marked variation trends across and along the fault zone. The microscale, fabric-related structural anisotropy generated during the early deformation phases appears to control the bulk pore size distribution, promoting the development of bimodal porosity systems. Accordingly, the background primary (sedimentary) matrix pore network is overprinted by a secondary (tectonic) pore network composed of microcracks located along the preexisting microfabric discontinuities. The cementation patterns of pervasive Fe-sulphide impregnation halos in the inner parts of fault zones reflect enhanced dilation-related fluid circulation in the early intermediate phases of growth faulting. These results may have important practical implications, for instance in terms of fault-seal analysis (e.g. vertical-lateral connectivity of sandstone wedges and fault blocks, structural-stratigraphy of half-graben reservoirs) and geophysical visualization of (sub)seismic fault zones (e.g. higher densities due to Fe-sulphide impregnation and consequent higher impedance of cores and inner damage zones), routinely performed in hydrocarbon exploration and production.

This growth fault system is inferred to develop in the prodelta region of a large Triassic delta system, prograding northwestward against and atop a regional palaeo-bathymetric high that was approximately oriented NE-SW. These faults are inferred to be responsible for the creation of palaeo-bathymetric relief atop the Botneheia Formation during the deposition of the Tschermakfjellet Fm, which favoured localized depozones (i.e. half-grabens) and consequent differential compaction, and thus preconditioning the formation of the lower order faults. The spatial arrangement, geometric relationships and infilling history of these half-grabens, and the internal sedimentary growth wedges also testify to an overall landward (i.e. counter-regional) growth faulting style with respect to the N-NW-directed progradation direction inferred for the associated delta systems. In such a setting, deep-rooted tectonic faults (Carboniferous) that bound the topographic high were likely reactivated by far-field tectonics related to the late Triassic Uralide orogeny to the E. This acted in synergy with regional differential compaction that created a landward-moving subsidence front sustaining a gently inclined, long-lived delta-facing slope. This slope instability in turn triggered shallow gravitational deformation and local depocentres, creating structurally controlled sand-mud accumulations, which also record detailed, climatically controlled variations of deltaic sediment supply redistribution and relative sea-level variations.

ACKNOWLEDGEMENTS

This study is part of the Petromaks Trias North Project (grant 234152/E30); we extend gratitude to the projects financial supporters, the Research Council of Norway and industry partners, Edison Norway, Lundin Norway, RWE Dea Norge, Statoil and Tullow Oil. Our many discussions with Snorre Olaussen, Kim Senger, Elisabeth Miller, Elisabeth Olsen, Luka Blažić, Beyene Haile, Tore Grane Klausen and Helge Hellevang during the field campaigns enriched the work. Moreover, we would like to deeply thank the Editor Atle Rotevatn and the referees Jack Williams, Thibault Cavailhes and Tore Grane Klausen for their accurate and constructive reviews.

REFERENCES

Allen, J. R. L. (1982). *Sedimentary structures: Their character and physical basis*, Vol. *657*. Amsterdam, the Netherlands: Elsevier.

Anell,I., Braathen, A., & Olaussen, S. (2014). Regional constraints of the Sørkapp Basin: A Carboniferous relic or a Cretaceous depression? *Marine and Petroleum Geology*, *54*, 123–138. https://doi.org/10.1016/j.marpetgeo.2014.02.023

Anell, I., Braathen, A., Olaussen, S., & Osmundsen, P. T. (2013). Evidence of faulting contradicts a quiescent northern Barents Shelf during the Triassic. *First Break*, *31*(6), 67–76.

Anell, I., Faleide, J. I., & Braathen, A. (2016). Regional tectonosedimentary development of the highs and basins of the northwestern Barents Shelf. *Norwegian Journal of Geology*, *96*, 27–41.

Armstrong, C., Mohrig, D., Hess, T., George, T., & Straub, K. M. (2014). Influence of growth faults on coastal fluvial systems: Examples from the late Miocene to Recent Mississippi River Delta. *Sedimentary Geology*, *301*, 120–132. https://doi.org/10.1016/j.sedgeo.2013.06.010

Back, S., Jing, T. H., Thang, T. X., & Morley, C. K. (2005). Stratigraphic development of synkinematic deposits in a large growth-fault system, onshore Brunei Darussalam. *Journal of the Geological Society London*, *162*, 243–258. https://doi.org/10.1144/0016-764903-006

Back, S., & Morley, C. (2016). Growth faults above shale – Seismic-scale outcrop analogues from the Makran foreland, SW Pakistan. *Marine and Petroleum Geology*, *70*, 144–162. https://doi.org/10.1016/j.marpetgeo.2015.11.008

Bally, A. W., Bernoulli, D., Davis, G. A., & Montadert, L. (1981). Listric normal faults. *Oceanologica Acta*, *4*, 87–101.

Balsamo, F., Bezerra, F. H., Vieira, M., & Storti, F. (2013). Structural control on the formation of iron oxide concretions and Liesegang bands in faulted, poorly lithified Cenozoic sandstones of the Paraiba basin, Brazil. *Geological Society of America Bulletin*, *125*, 913–931. https://doi.org/10.1130/B30686.1

Bense, V. F., & Person, M. A. (2006). Faults as conduit-barrier systems to fluid flow in siliciclastic sedimentary aquifers. *Water Resources Research*, *42*, W05421.

Bhattacharya, J. P., & Davies, R. K. (2001). Growth faults at the prodelta to delta-front transition, Cretaceous Ferron sandstone, Utah. *Marine and Petroleum Geology*, *18*, 525–534. https://doi.org/10.1016/S0264-8172(01)00015-0

Bolton, A. J., Maltman, A. J., & Fisher, Q. (2000). Anisotropic permeability and bimodal pore-size distributions of fine-grained marine sediments. *Marine and Petroleum Geology*, *17*, 657–672. https://doi.org/10.1016/S0264-8172(00)00019-2

Bouroullec, R., Cartwright, J. A., Johnson, H. D., Lansigu, C., Quémener, J.-M., & Savanier, D. (2004). Syndepositional faulting in the Grès d'Annot Formation, SE France: High-resolution kinematic analysis and stratigraphic response to growth faulting. *Geological Society, London, Special Publications*, *221*, 241–265. https://doi.org/10.1144/gsl.sp.2004.221.01.13

Braathen, A., Bergh, S. G., & Maher, H. D. (1997). Thrust kinematics in the central part of the Tertiary transpressional fold-thrust belt in Spitsbergen. *NGU Bulletin*, *433*, 32–33.

Braathen, A., Maher, H. D., Haabet, T. E., Kristensen, S. E., Tørudbakken, B. O., & Worsley, D. (1999). Caledonian thrusting on Bjornoya: Implications for Palaeozoic and Mesozoic tectonism of the western Barents Shelf. *Norsk Geologisk Tidsskrift*, *79*(1), 57–68. https://doi.org/10.1080/002919699433915

Braathen, A., Midtkandal, I., Mulrooney, M. J., Appleyard, T. R., Haile, B. G., & Yperen, A. E. (2017). Growth-faults from delta collapse – structural and sedimentological investigation of the Last Chance delta, Ferron Sandstone, Utah. *Basin Research*, 1–20. https://doi.org/10.1111/bre.12271

Braathen, A., Osmundsen, P. T., & Gabrielsen, R. H. (2004). Dynamic development of fault rocks in a crustal-scale detachment: An example from western Norway. *Tectonics*, *23*, 1–27.

Braathen, A., Osmundsen, P. T., Hauso, H., Semshaug, S., Fredman, N., & Buckley, S. J. (2013). Fault-induced deformation in a poorly consolidated, siliciclastic growth basin: A study from the Devonian in Norway. *Tectonophysics*, *586*, 112–129. https://doi.org/10.1016/j.tecto.2012.11.008

Braathen, A., Tveranger, J., Fossen, H., Skar, T., Cardozo, N., Semshaug, S. L., … Sverdrup, E. (2009). Fault facies as concept and its applications to sandstone reservoirs. *American Association for Petroleum Geologists Bulletin*, *93*, 891–917. https://doi.org/10.1306/03230908116

Caine, J. S., Evans, J. P., & Forster, C. B. (1996). Fault zone architecture and permeability structure. *Geology*, *24*(11), 1025–1028. https://doi.org/10.1130/0091-7613(1996)024<1025:FZAAPS>2.3.CO;2

Callot, P., Odonne, F., Debroas, E.-J., Maillard, A., Dhont, D., Basile, C., & Hoareau, G. (2009). Three-dimensional architecture of submarine slide surfaces and associated soft-sediment deformation in the Lutetian Sobrarbe deltaic complex (Ainsa, Spanish Pyrenees). *Sedimentology*, *56*, 1226–1249. https://doi.org/10.1111/j.1365-3091.2008.01030.x

Cavailhes, T., Sizun, J.-P., Labaume, P., Chauvet, A., Buatier, M., Soliva, R., … Gout, C. (2013). Influence of fault rock foliation on fault zone permeability: The case of deeply buried arkosic sandstones (Grès d'Annot, southeastern France). *AAPG Bulletin*, *97/9*, 1521–1543. https://doi.org/10.1306/03071312127

Cohen, H. A., & McClay, K. R. (1996). Sedimentation and shale tectonics of the nortwestern Niger Delta front. *Marine and Petroleum Geology*, *13*, 313–328. https://doi.org/10.1016/0264-8172(95)00067-4

Corfu, F., Andersen, T. B., & Gasser, D. (2014). The Scandinavian Caledonides: Main features, conceptual advances, and critical questions. In: F. Corfu, T. B. Andersen & D. Gasser (Eds.), *New perspectives on the caledonides of Scandinavia and related areas* (pp. 9–43). London: Geological Society, Special Publications, 390.

Dallmann, W. K., Dypvik, H., Gjelberg, J. G., Harland, W. B., Johannessen, E. P., Keilen, H. B., … Worsley, D. (1999) *Lithostratigraphic Lexicon of Svalbard: Review and recommendations for nomenclature use*, 318 pp. Tromsø, Norway: Norsk Polarinstitutt.

Damuth, J. E. (1994). Neogene gravity tectonics and depositional processes on the deep Niger Delta continental margin. *Marine and Petroleum Geology*, *11*, 320–346. https://doi.org/10.1016/0264-8172(94)90053-1

Edwards, M. B. (1976). Growth faults in upper Triassic deltaic sediments, Svalbard. *AAPG Bulletin*, *60*, 341–355.

Faleide, J. I., Tsikalas, F., Breivik, A. J., Mjelde, R., Ritzmann, O., Engen, O., … Eldholm, O. (2008). Structure and evolution of the continental margin off Norway and the Barents Sea. *Episodes*, *31*, 82–91.

Fleming, E. J., Flowerdew, M. J., Smyth, H. R., Scott, R. A., Morton, A. C., Omma, J. E., … Whitehouse, M. J. (2016). Provenance of Triassic sandstones on the southwest Barents Shelf and the implication for sediment dispersal patterns in northwest Pangaea. *Marine and Petroleum Geology*, *78*, 516–535. https://doi.org/10.1016/j.marpetgeo.2016.10.005

Fossen, H. (2010). Deformation bands formed during soft- sediment deformation: Observations from SE Utah. *Marine and Petroleum Geology*, *27*, 215–222. https://doi.org/10.1016/j.marpetgeo.2009.06.005

Fossen, H., Schulz, R. A., Shipton, Z. K., & Mair, K. (2007). Deformation Bands in Sandstone – a Review. *The Geological Society of London*, *164*, 755–769. https://doi.org/10.1144/0016-76492006-036

Gabrielsen, R. H., Sokoutis, D., Willingshofer, D., & Faleide, J. I. (2016). Fault linkage across weak layers during extension: An experimental approach with reference to the Hoop Fault Complex of the SW Barents Sea. *Petroleum Geoscience*, *22*, 123–135. https://doi.org/10.1144/petgeo2015-029

Gagliano, M. S. (2005). Effects of geological faults on levee failures in South Louisiana. In: Testimony of Sherwood Gagliano. Ph.D. U.S. Senate Committee on Environment and Public Works, Senator James M. Inhofe, Chairman, Washington, D.C., pp. 1–28.

Haile, B. G., Klausen, T. G., Czarniecka, U., Xi, K., Jahren, J., & Hellevang, H. (2018). How are diagenesis and reservoir quality linked to depositional facies? A deltaic succession, Edgeøya, Svalbard *Marine and Petroleum Geology*, *92*, 519–546. https://doi.org/10.1016/j.marpetgeo.2017.11.019

Hancock, P. L., & Bevan, T. G. (1987). Brittle modes of foreland extension . In P. Coward, J. F. Dewey & P. L. Hancock (Eds.), *Continental extensional tectonics* (pp. 127–137). London: Geological Society, Special Publications, 28. https://doi.org/10.1144/GSL.SP.1987.028.01.10

Harland, W. B. (1997). Proto-basement in Svalbard. *Polar Research*, *16*, 123–147. https://doi.org/10.3402/polar.v16i2.6631

Heynekamp, M. R., Goodwin, L. B., Mozley, P. S., & Haneberg, W. C. (1999). Controls on fault-zone architecture in poorly lithified sediments, Rio Grande Rift, New Mexico: Implications for fault-zone permeability and fluid flow. In W. C. Haneberg, P. S. Mozley, J. Casey Moore & L. B. Goodwin (Eds.), *Faults and subsurface fluid flow in the shallow crust*, Vol. *113* (pp. 27–51). Washington, DC: AGU Geophysical Monograph. American Geophysical Union. https://doi.org/10.1029/GM113

Hurum, J. H., Roberts, A. J., Nakrem, H. A., Stenløkk, J. A., & Mørk, A. (2014). The first recovered ichthyosaur from the Middle Triassic of Edgeøya, Svalbard. *Norwegian Petroleum Directorate Bulletin*, *11*, 97–110.

Imber, J., Childs, C., Nell, P. A. R., Walsh, J. J., Hodgetts, D., & Flint, S. (2003). Hanging wall fault kinematics and footwall collapse in listric growth fault systems. *Journal of Structural Geology*, *25*(2), 197–208. https://doi.org/10.1016/S0191-8141(02)00034-2

King, R. C., Backé, G., Morley, C. K., Hillis, R. R., & Tingay, M. R. P. (2010). Balancing deformation in NW Borneo: Quantifying plate-scale vs. gravitational tectonics in a delta and deepwater fold-thrust belt system. *Marine and Petroleum Geology*, *27*(1), 238–246. https://doi.org/10.1016/j.marpetgeo.2009.07.008

Klausen, T., & Mørk, A. (2014). The upper Triassic paralic deposits of the De Geerdalen formation on hopen: Outcrop analog to the subsurface snadd formation in the Barents Sea. *AAPG Bulletin*, *98*, 1911–1941. https://doi.org/10.1306/02191413064

Klausen, T. G., Müller, R., Slama, J., & Helland-Hansen, W. (2016). Evidence for Late Triassic provenance areas and Early Jurassic sediment supply turnover in the Barents Sea Basin of northern Pangea. *Lithosphere*, *9*(1), 14–28.

Klausen, T. G., Ryseth, A. E., Helland-Hansen, W., Gawthorpe, R., & Laursen, I. (2014). Spatial and temporal changes in geometries of fluvial channel bodies from the Triassic Snadd Formation of offshore Norway. *Journal of Sedimentary Research*, *84*, 567–585. https://doi.org/10.2110/jsr.2014.47

Klausen, T. G., Ryseth, A. E., Helland-Hansen, W., Gawthorpe, R., & Laursen, I. (2015). Regional development and sequence stratigraphy of the middle to late Triassic snadd formation, Norwegian Barents Sea. *Marine and Petroleum Geology*, *62*, 102–122. https://doi.org/10.1016/j.marpetgeo.2015.02.004

Krajewski, K. P. (2011). Phosphatic microbialites in the Triassic phosphogenic facies of Svalbard. In V. C. Tewari & J. Seckbach (Eds.), *Stromatolites: Interaction of microbes with sediments. Cellular origin, life in extreme habitats and astrobiology*, vol. *18* (pp. 187–222). Springer. https://doi.org/10.1007/978-94-007-0397-1_9

Krajewski, K. P. (2013). Organic matter–apatite–pyrite relationships in the Botneheia Formation (Middle Triassic) of eastern Svalbard: Relevance to the formation of petroleum source rocks in the NW Barents Sea shelf. *Marine and Petroleum Geology*, *45*, 69–105. https://doi.org/10.1016/j.marpetgeo.2013.04.016

León Y León, C. A. (1998). New perspectives in mercury porosimetry. *Advances in Colloid and Interface Science*, *76–77*, 341–372. https://doi.org/10.1016/S0001-8686(98)00052-9

Lohr, T., Krawczyk, C., Oncken, O., & Tanner, D. (2008). Evolution of a fault surface from 3D attribute analysis and displacement measurements. *Journal of Structural Geology*, *30*(6), 690–700. https://doi.org/10.1016/j.jsg.2008.02.009

Loveless, S., Bense, V., & Turner, J. (2011). Fault deformation processes and permeability architecture within recent rift sediments, central Greece. *Journal of Structural Geology*, *33*, 1554–1568.

Lyberis, N., & Manby, G. (1999). Continental collision and lateral escape deformation in the lower and upper crust: An example from Caledonide Svalbard. *Tectonics*, *18*(1), 40–63. https://doi.org/10.1029/1998TC900013

Maestro, A., Barnolas, A., Somoza, L., Lowrie, A., & Lawton, T. (2002). Geometry and structure associated to gas-charged sediments and recent growth faults in the Ebro Delta (Spain). *Marine Geology*, *186*, 351–368. https://doi.org/10.1016/S0025-3227(02)00212-8

Maher, H. D. (2001). Manifestations of the cretaceous high arctic large igneous province in Svalbard. *The Journal of Geology*, *109*(1), 91–104. https://doi.org/10.1086/317960

Maher, H. D., Ogata, K., & Braathen, A. (2017). Cone-in-cone and beef mineralization associated with Triassic growth basin faulting and shallow shale diagenesis, Edgeøya, Svalbard. *Geological Magazine*, *154*(2), 201–216. https://doi.org/10.1017/S0016756815000886

Mandl, G., & Crans, W. (1981). Gravitational Gliding in Deltas. In K. R. McClay & N. J. Price (Eds.), *Thrust and nappe tectonics* (pp. 41–54). London: Geological Society, Special Publications, 9.

Marello, L., J. Ebbing, J., & Gernigon, L. (2013). Basement inhomogeneities and crustal setting in the Barents Sea from a combined 3D gravity and magnetic model. *Geophysical Journal International*, *193/2*, 557–584. https://doi.org/10.1093/gji/ggt018

McClay, K. R., Dooley, T., & Lewis, G. (1998). Analog modelling of progradational delta systems. *Geology*, *26*(9), 771–774. https://doi.org/10.1130/0091-7613(1998)026<0771:AMOPDS>2.3.CO;2

McClay, K. R., & Ellis, K. R. (1987). Geometries of extensional fault systems developed in model experiments. *Geology*, *15*, 341–344. https://doi.org/10.1130/0091-7613(1987)15<341:GOEFSD>2.0.CO;2

Meng, Q., Hooker, J., & Cartwright, J. (2017). Early overpressuring in organic-rich shales during burial: Evidence from fibrous calcite veins in the Lower Jurassic Shales-with-Beef Member in the Wessex Basin, UK. *Journal of the Geological Society*, *174*, 869–882. https://doi.org/10.1144/jgs2016-146

Minakov, A., Faleide, J. I., Glebovsky, V. Y., & Mjelde, R. (2012). Structure and evolution of the northern Barents-Kara Sea continental margin from integrated analysis of potential fields, bathymetry and sparse seismic data. *Geophysical Journal International*, *188*, 79–102. https://doi.org/10.1111/j.1365-246X.2011.05258.x

Mitterer, R. M. (2010). Methanogenesis and sulfate reduction in marine sediments: A new model. *Earth and Planetary Science Letters*, *295*, 358–366. https://doi.org/10.1016/j.epsl.2010.04.009

Mørk, A., Dallman, W. K., Dypvik, H., Johannessen, E. P., Larssen, G. B., Nagy, J., … Worsley, D. (1999). Mesozoic lithostratigraphy. In W. K. Dallman (Ed.), *Lithostratigraphic lexicon of Svalbard. Upper Palaeozoic to Quaternary bedrock. Review and recommendations for nomenclature use* (pp. 127–214). Tromsø, Norway: Norsk Polarinstitutt.

Mozley, P. S., & Goodwin, L. B. (1995). Patterns of cementation along a Cenozoic normal fault: A record of paleoflow orientations.

Geology, *23*, 539–542. https://doi.org/10.1130/0091-7613(1995)023<0539:POCAAC>2.3.CO;2

Nejbert, K., Krajewski, K. P., Dubinska, E., & Pecskay, Z. (2011). Dolerites of Svalbard, north-west Barents Sea Shelf: Age, tectonic setting and significance for geotectonic interpretation of the High-Arctic Large Igneous Province. *Polar Research*, *30*(7306), 1–24.

Nemec, W., Steel, R. J., Gjelberg, J., Collinson, J. D., Prestholm, E., Øxnevad, I. E., & Worsley, D. (1988). Exhumed rotational slides and scar infill features in a Cretaceous delta front, eastern Spitsbergen. *Polar Research*, *6*, 105–112. https://doi.org/10.3402/polar.v6i1.6850

Nøttvedt, A., Cecchi, M., Gjelberg, J. C., Kristensen, S. E., Lønøy, A., Rasmussen, A., … van Veen, P. M. (1992). Svalbard-Barents Sea correlation: A short review. In T. Vorren, E. Bergsager, Ø. A. Dahl-Stamnes, E. Holter, E. Johansen, B. Lie & T. B. Lund (Eds.), *Arctic geology and petroleum potential* (pp. 15–17). Amsterdam, the Netherlands: Elsevier, Norwegian Petroleum Society, Special Publication 2.

Onderdonk, N., & Midtkandal, I. (2010). Mechanisms of collapse of the Cretaceous Helvetiafjellet Formation at Kvalvagen, Eeastern Spitsbergen. *Marine and Petroleum Geology*, *27*, 2118–2140. https://doi.org/10.1016/j.marpetgeo.2010.09.004

Osmundsen, P. T., Braathen, A., Rød, R. S., & Hynne, I. B. (2014). Styles of normal faulting and fault-controlled sedimentation in the Triassic deposits of Eastern Svalbard. *Norwegian Petroleum Directorate Bulletin*, *11*, 61–69.

Panpichityota, N., Morley, C. K., & Ghosh, J. (2018). Link between growth faulting and initiation of a mass transport deposit in the northern Taranaki Basin, New Zealand. *Basin Research*, *30*(2), 237–248. https://doi.org/10.1111/bre.12251

Pochat, S., Castelltort, S., vanden Driessche, J., Besnard, K., & Gumiaux, C. (2004). A simple method of determing sand / shale ratios from seismic analysis of growth faults: An example from Upper Oligocene to Lower Miocene Niger Delta deposits. *American Association of Petroleum Geologists Bulletin*, *88*, 1357–1367. https://doi.org/10.1306/04290403117

Pochat, S., & van den Driesse, J. (2007). Impact of synsedimentary metre-scale normal fault scarps on sediment gravity flow dynamics: An example from the Grès d'Annot Formation, SE France. *Sedimentary Geology*, *202*, 796–820. https://doi.org/10.1016/j.sedgeo.2007.09.005

Rawling, G., & Goodwin, L. (2003). Cataclasis and particulate flow in faulted, poorly lithified sediments. *Journal of Structural Geology*, *25*, 317–331. https://doi.org/10.1016/S0191-8141(02)00041-X

Rawling, G., & Goodwin, L. (2006). Structural record of the mechanical evolution of mixed zones in faulted poorly lithified sediments, Rio Grande rift, New Mexico, USA. *Journal of Structural Geology*, *28*, 1623–1639. https://doi.org/10.1016/j.jsg.2006.06.008

Rider, M. H. (1978). Growth faults in Carboniferous of Western Ireland. *AAPG Bulletin*, *62*, 2191–2213.

Rittersbacher, A., Howell, J., & Buckley, S. J. (2014). Analysis of fluvial architecture in the Blackhawk formation, Wasatch plateau, Utah, U.S.A., using large 3D photo- realistic models. *Journal of Sedimentary Research*, *84*, 72–87. https://doi.org/10.2110/jsr.2014.12

Rød, R. S., Hynne, I. B., & Mørk, A. (2014). Depositional environment of the Upper Triassic De Geerdalen Formation–an EW Transect from Edgeøya to Central Spitsbergen, Svalbard. *Norwegian Petroleum Directorate Bulletin*, *11*, 21–40. Stavanger 2014, ISSN Online 1894-7670, ISBN 978-82-7257-117-6.

Rouby, D., Raillard, S., Guillocheau, F., Bouroullec, R., & Nalpas, T. (2002). Kinematics of a growth fault/raft system on the West African margin using 3-D restoration. *Journal of Structural Geology*, *24*(4), 783–796. https://doi.org/10.1016/S0191-8141(01)00108-0

Rutter, E. (1986). On the nomenclature of mode of failure transitions in rocks. *Tectonophysics*, *122*, 381–387. https://doi.org/10.1016/0040-1951(86)90153-8

Sapin, F., Ringenbach, J.-C., Rives, T., & Pubellier, M. (2012). Counter-regional normal faults in shale- dominated deltas: Origin, mechanism and evolution. *Marine and Petroleum Geology*, *37*, 121–128. https://doi.org/10.1016/j.marpetgeo.2012.05.001

Scott, R. A., Howard, J. P., Guo, L., Schekoldin, R., & Pease, V. (2011). Offset and curvature of the Novaya Zemlya fold-and-thrust belt, Arctic Russia. *Geological Society, London, Petroleum Geology Conference Series*, *7*, 645–657. https://doi.org/10.1144/0070645

Senger, K., Tveranger, J., Ogata, K., Braathen, A., & Planke, S. (2014). Late Mesozoic magmatism in Svalbard: A review. *Earth Science Reviews*, *139*, 123–144. https://doi.org/10.1016/j.earscirev.2014.09.002

Sibson, R. H. (1977). Fault rocks and fault mechanisms. *Journal of the Geological Society*, *133*(3), 191–213. https://doi.org/10.1144/gsjgs.133.3.0191

Smyrak-Sikora, A., Osmundsen, P. T., Braathen, A., Ogata, K., Anell, I., Husteli, B., … Olaussen, S. (2017). Sedimentary architecture of siliciclastic, syntectonic graben and half-graben fill in Kvalpynten, Edgeøya, Svalbard. Norsk Geologisk Vinterkonferanse. January 2017.

Steel, R., Gjelberg, J., Nøttvedt, A., Helland-Hansen, W., Kleinspehn, K. L., & Rye Larsen, M. (1985). The Tertiary strike slip basins and orogenic belt of Spitsbergen. In K. T. Biddle & N. Christie-Blick (Eds.), *Strike-slip deformation, basin formation, and sedimentation* (pp. 339–359). Society of Economic Paleontologists and Mineralogists, Special Publication 37.

Torabi, A., Fossen, H., & Braathen, A. (2013). Insight into petrophysical properties of deformed sandstone reservoirs. *American Association of Petroleum Geologists Bulletin*, *97*, 619–637. https://doi.org/10.1306/10031212040

Tugarova, M. A., & Fedyaevsky, A. G. (2014). Calcareous microbialites in the Upper Triassic succession of Eastern Svalbard. *Norwegian Petroleum Directorate Bulletin*, *11*, 137–152.

Vigran, O. S., Mangerud, G., Mørk, A., Worsley, D., & Hochuli, P. A. (2014). Palynology and geology of the Triassic succession of Svalbard and the Barents Sea. *Geological Survey of Norway Special Publications*, *14*, 270.

Washburn, E. W. (1921). Note on a method of determining the distribution of pore sizes in a porous material. *Proceedings of the National Academy of Sciences of the United States of America*, *7*, 115–116. https://doi.org/10.1073/pnas.7.4.115

Wignall, P. B., & Best, J. L. (2004). Sedimentology and kinematics of a large, retrogressive growth-fault system in Upper Carboniferous deltaic sediments, western Ireland. *Sedimentology*, *51*, 1343–1358. https://doi.org/10.1111/j.1365-3091.2004.00673.x

Yeager, K. M., Brunner, C. A., Kulp, M. A., Fischer, D., Feagin, R. A., Schindler, K. J., … Bera, G. (2012). Significance of active growth faulting on marsh accretion processes in the lower Pearl River, Louisiana. *Geomorphology*, *153*, 127–143. https://doi.org/10.1016/j.geomorph.2012.02.018

Zecchin, M., Massari, F., Mellere, D., & Prosser, G. (2003). Architectural styles of prograding wedges in a tectonically active setting, Crotone Basin, Southern Italy. *Journal of the Geological Society, London*, *160*, 863–880. https://doi.org/10.1144/0016-764902-099